Characterizing thin clouds using aerosol optical depth information

Master's Thesis

in Atmospheric Sciences

Submitted to the
Faculty of Geo- and Atmospheric Sciences
of the
University of Innsbruck

in partial fulfillment of the requirements for the degree of
Master of Science

by
Sophie Stuke

Advisors

Ao. Univ.-Prof. Dr. Mario Blumthaler,
Univ.-Prof. em. Dr. Michael Kuhn

Innsbruck, November 2016

Abstract

Based on direct solar irradiance measurements, this thesis tries to infer optical properties of clouds. Measurements have been collected in Innsbruck, Austria, using a precision filter radiometer (PFR) with four wavelength channels at 368, 412, 501 and 861 nm. Routinely, these measurements are used to infer aerosol properties, like aerosol optical depth (AOD) or the Ångström exponent α. Operational aerosol retrievals are only possible during situations when no clouds are present in the field-of-view of the PFR. Therefore, only a limited number of direct solar irradiance measurements with clouds obscuring the sun (i.e., *cloud-contaminated* measurements) have been used for any analysis so far.

This unused dataset of cloud-contaminated measurements, taken from 2007 to 2014, is used to derive cloud optical depth (COD). In order to achieve this, a straightforward approach is employed: Extinction by NO_2, O_3 and Rayleigh scattering are taken into account in the retrieval of the optical depth (OD) for cloud-contaminated measurements. However, the derived OD is influenced by both the presence of aerosols and clouds obscuring the sun (i.e., OD = COD + AOD), while other contributors are neglected. The influence of the AOD on single measurements is estimated by using a daily mean value of AOD retrievals of the same day (gathered by the PFR during cloud-free conditions), or the previous day, if no AOD retrievals are available on the specific day. This approach is valid because variation of aerosol properties and cloud optical properties exhibit different time scales. The COD is calculated by subtracting the daily mean AOD value from single OD retrievals (i.e., COD = OD − mean(AOD)).

Derived COD values range from 0.10 to 2.64. Therefore, only optically thin clouds with a COD below three can be investigated using the proposed approach. The COD retrievals exhibit an uncertainty because of using the mean AOD in the derivation: the AOD (501 nm) can vary by up to 0.2 on specific days and employing the daily mean value of AOD does not account for this variability. Based on the spectral COD retrievals using the four channels of the PFR and employing Ångström's turbidity formula, the Ångström parameter α and the curvature parameter γ are derived. The parameter α exhibits a value range from -0.82 to 1.99 with the 10^{th}-precentile at -0.23 and the 90^{th}-precentile at 0.10 for cloud-contaminated measurements. The curvature parameter γ exhibits a value range from -3.02 to 6.52 with a mean of 0.02. However, the 10^{th}-percentile is at -0.06 and the 90^{th}-percentile at 0.09, i.e. for the majority of the retrievals γ is nearly zero. Therefore, it is not further taken into account.

Based on hourly all-sky images, the cloud types obscuring the sun during specific measurements are determined for the period from 2011 to 2013 by manual inspection. However, events are only taken into account if (i) the solar disc is covered by a single cloud type, (ii) the solar zenith angle is not too high to avoid contamination by dif-

ferent cloud types along the slanted path through the atmosphere, and, (iii) at least two consecutive all-sky images show the same cloud type. Only Cirrus (Ci), Cirrostratus (Cs), Stratocumulus (Sc) and Altocumulus (Ac) clouds are analyzed in detail because for other cloud types too few events have been recognized (e.g., only 3 events for Stratus). Cirrus clouds show a COD range from 0.17 to 0.72 with an Ångström parameter between -0.20 and -0.04. The other cloud types' value ranges for COD are comparable: 0.21 to 1.84 for Cs, 0.40 to 2.37 for Sc and 0.17 to 2.19 for Ac. Ångström exponents range from -0.22 to 0.02 for Cs, -0.36 to 0.05 for Sc and -0.33 to -0.05 for Ac.

The analyzed ice clouds (Ci, Cs) and liquid water clouds (Sc, Ac) exhibit differences in the respective COD-α-relations. Values for Ci cluster in a narrow region for both parameters with a mean COD of 0.4 and a mean α of -0.1. Cirrostratus clouds show α values also with a mean of -0.1, but approximately constant over the whole COD range. However, water clouds (Sc, Ac) show a decreasing α with increasing COD, down to -0.3 for COD ≈ 2.3. It is hypothesized, that the less negative Ångström exponents of ice clouds arise from the weaker spectral dependence of the extinction efficiency for typical Ci and Cs ice crystal habits and sizes in the VIS and NIR spectral range. The spectral variability of extinction efficiency for water clouds is higher than for ice clouds in these wavelength ranges, yielding more negative α values. Moreover, multiple scattering within water clouds is hypothesized to further increase this difference.

Contents

1 Introduction

Clouds play a profound role in the radiation budget of the earth and influence the climate system by redistributing heat and moisture (e.g., Wielicki et al. 1995; Shupe et al. 2016). Additionally, clouds act as a crucial link in the hydrological cycle. However, the impact of clouds on the earth-atmosphere radiation balance is not fully understood (Forster et al. 2007). Cloud-climate feedbacks influence the radiative budget on both large and small scales (Stephens 2005) and have been assigned as a leading source of uncertainty in understanding global climate sensitivity (IPCC 2007). Especially the influence of ice clouds is uncertain and their effects on the climate system are not well understood (e.g., Stephens et al. 1990; Tian and Ramanathan 2002), although they can cover up to 40% of the globe and influence radiation in both the shortwave and longwave spectrum (Raschke 1993). In turn, clouds are affected by large-scale atmospheric circulation patterns, the presence of aerosols, atmosphere-surface interaction and thermodynamic processes in the troposphere (Shupe et al. 2016). The most important parameters determining the radiative impact of clouds are cloud fraction, cloud albedo, the extinction coefficient b and its vertical integral, cloud optical depth τ_c (COD) (Matrosov et al. 2003; Sourdeval et al. 2015). COD is an indication of the cloud opacity for a given wavelength of radiation (Turner et al. 2007), however it is rather insensitive to the wavelength within the shortwave solar spectrum (Comstock and Sassen 2001). Typical values for τ_c range from <1 to over 100 (Stephens 1994; Lohmann et al. 2016).

Clouds are characterized by a high spatial and temporal variability of various properties including, for example, cloud cover, cloud depth, cloud particle size distribution. These variabilities affect measurements (Boers et al. 2000) and are insufficiently represented in global climate models (GCMs). GCMs have become more and more sophisticated in recent years and are able to model clear-sky shortwave and longwave fluxes in good agreement with measurements if adequate information about aerosol properties, surface albedo and water vapor is included in the model calculations (Turner et al. 2004; Michalsky et al. 2006). However, they still struggle in predicting macrophysical, microphysical and optical properties of clouds and, therefore, in predicting shortwave and longwave radiative fluxes under broken or overcast conditions (Bender et al. 2006; Zhang et al. 2005; Turner et al. 2007). Modelling of cloudy-sky radiative fluxes requires information about cloud optical thickness, scattering processes within the cloud (depending on hydrometeor shape and phase), cloud cover and cloud inhomogeneity (Comstock et al. 2007). GCMs use parametrizations of microphysical properties in order to calculate radiative characteristics of clouds.

Cloud radiative properties are influenced by both macro- and microphysical parameters (Matrosov et al. 2003). The former include, for example, cloud base and top height, horizontal cloud extent and cloud temperature, while the latter include cloud particle size, shape and phase. Measurements of macrophysical properties can be obtained using LIDAR, radar or radio soundings (Comstock and Sassen 2001), while microphysical properties can be derived using a multitude of retrieval techniques including remote sensing, airborne in-situ and ground-based measurements (e.g., Vogelmann et al. 2012).

An understanding of cloud physics and their influence on the radiative budget via cloud-climate feedbacks (Wielicki et al. 1995) is crucial in improving numerical earth system modeling abilities and to develop and improve parametrizations of cloud effects in GCMs (Shupe et al. 2016). Therefore, estimates of the optical depth of different cloud types are desirable to design and validate parametrizations. However, especially the retrieval of radiative and microphysical properties of *optically thin* clouds do show large differences when different retrieval methods are used (Comstock et al. 2007; Turner et al. 2007). Moreover, the definition of *optically thin* clouds is somewhat ambiguous in literature. For example, Comstock et al. (2007) associate optically thin cirrus clouds with $\tau_c < 0.3$, while Segal-Rosenheimer et al. (2013) use $\tau_c < 1$ as a threshold for the same type of clouds. Turner (2005) associate optically thin clouds with a threshold of $\tau \leq 6$, while Wang and Min (2008) use $\tau \leq 10$.

Estimates of cloud optical depth rely on several measurement systems. Ground-based measurements of spectral or broadband downward radiative fluxes are related to cloud transmittances and are used to derive cloud optical depth (e.g., Leontieva and Stamnes 1994; Boers 1997; Barker et al. 1998; Boers et al. 2000), while spaceborne observations rely on radiation reflected by clouds to derive cloud optical depth (e.g., Rossow and Schiffer 1991; Barker and Liu 1995; Loeb and Coakley 1998). Spaceborne observation systems include the Moderate-resolution Imaging Spectroradiometer (MODIS) or the Cloud-Aerosol Lidar and Infrared Pathfinder Satellite Observations (CALIPSO) satellite platform.

Most retrieval techniques assume single-dimensional, plane-parallel radiative transfer through the atmosphere (Beaulne et al. 2005) and are influenced by the solar zenith angle, aerosol optical thickness (AOD), abundances of water vapor and ozone, cloud particle effective radius, the fraction of ice and water within the cloud and inhomogeneities in cloud cover as well as within the cloud (Barnard and Long 2004). Ground-based measurements are less sensitive to uncertainties in cloud droplet-size distribution (Rawlins and Foot 1990). However, a disadvantage of ground-based measurements is that they might represent very local estimates, due to the high spatial variability of clouds (Barker et al. 1998). Ground-based and spaceborne estimates for cloud optical depth can show different results when compared. Min and Harrison (1996) state that

they are in good agreement for optical depths below 10, but surface-based estimates are consistently larger (up to a factor of 2) for higher optical depths.

The broadband measurement of direct downward solar fluxes in the visible or near-infrared spectrum using pyranometers is the most commonly employed approach to derive COD. These instruments are standard equipment at many meteorological measurement sites. However, these retrievals are thought to work well only for overcast conditions, yielding an effective COD which assumes homogeneous cloud cover and cloud characteristics over the instrument's field-of-view (FOV) (Barker and Marshak 2001). Using sun photometers for spectral radiometric measurements of downward fluxes is another approach to derive cloud optical depth (e.g., Min and Harrison 1996; Leontieva and Stamnes 1996; Marshak et al. 2004). Marshak et al. (2004) used a combination of spectral zenith radiance measurements in the red and near-infrared spectral regions to derive cloud optical depth and cloud fraction. Chiu et al. (2010) used a similar approach with spectral zenith radiance measurements at 440 and 870 nm gathered by instruments of the Aerosol Robotic Network (AERONET).

AERONET was initially designed to retrieve optical and microphysical properties of aerosols using direct beam measurements of ground-based radiometers during clear-sky conditions (Holben et al. 1998). When the sun is obstructed by clouds, aerosol characteristics cannot be inferred using direct beam measurements. In these situations AERONET instruments switch in *cloud mode* to conduct zenith radiance measurements to retrieve cloud optical depth (Chiu et al. 2010).

In order to derive COD information more locally (i.e., COD valid for a single "sky element" and not an effective COD for the whole hemisphere), spectral direct-beam transmittances of solar radiation can be measured using a sun photometer with a sun tracker (Segal-Rosenheimer et al. 2013). These derived values are influenced by multiple forward scattering and are inversely proportional to the cosine of solar zenith angle θ (Barker and Marshak 2001). The FOV of a sun photometer usually exceeds the solar disc marginally. Contributions of scattered solar radiation into the instrument's FOV add onto the direct beam solar radiation. However, the derivation of the optical depth using a direct beam sun photometer assumes direct attenuation only. Therefore, with the presence of scattering particles (increasing the measured radiation by scattering *into* the instrument's FOV) the derived actual optical depth will be underestimated by these measurements. This underestimation is dependent on the degree to which the FOV exceeds the solar disc and the particle size of the scattering particles (Kinne et al. 1997). Additionally, strong forward scattering under cloudy conditions leads to an increase of incoming radiation in the instrument's FOV and, therefore, to an underestimation of total optical depth. If the cloud contribution is not taken into account, this will result in an overestimation of the AOD (Segal-Rosenheimer et al. 2013).

The herein presented work tries to infer cloud optical depth information for several cloud types using spectral direct solar irradiance measurements with clouds obscuring the sun gathered by a precision filter radiometer (PFR) in Innsbruck, Austria. However, the instrument used is initially intended to measure aerosol optical depth during clear-sky conditions (see Wuttke et al. 2012), comparable to the AERONET measurement devices used in the work of Chiu et al. (2010).

1.1 Motivation

Operational estimates of cloud optical depths using ground-based instruments are sparse, especially when it comes to global coverage. Chiu et al. (2010) state that, on the one hand, with the Atmospheric Radiation Measurement (ARM) program (Stokes and Schwartz 1994) and Cloudnet (Illingworth et al. 2007) only two operational networks provide continuous cloud measurements. However, the former includes five sites while the latter only includes three measurement sites. On the other hand, operational networks to measure aerosol properties have been developed, such as AERONET (Holben et al. 1998) or the Global Atmosphere Watch (GAW) program of the World Meteorological Organization (WMO). Aerosol measurement networks include more stations and, therefore, provide better coverage. These networks use spectral direct beam measurements of downward solar fluxes to determine AOD and other aerosol related properties. These aerosol properties can only be determined when the sun is not obscured by clouds. However, direct beam measurements are continuously gathered. Data from network stations such as AERONET are available for three data quality levels: Level 1.0 (unscreened), Level 1.5 (cloud-screened), and Level 2.0 (cloud-screened and quality-assured) (NASA cited 2016a). Therefore, huge amounts of data with clouds obscuring the sun (Level 1.0) are not used for AOD retrieval but are potentially available to derive cloud optical parameters.

An approach to derive COD information based on radiative measurements gathered by operational networks like AERONET, can be extremely beneficial for comparison with spaceborne estimates of COD and validation of cloud parameterizations used in numerical weather prediction (NWP) models. For example, Chiu et al. (2010) already used *cloud-contaminated* AERONET measurements to derive COD information.

Wuttke et al. (2012) used direct solar irradiance measurements at wavelengths of 368, 412, 501 and 861 nm gathered by a PFR in Innsbruck, Austria, from 2007 to 2011 to infer AOD information in a one minute temporal resolution. Measurements of AOD were only considered if the sun was not obstructed by clouds and the air mass was lower than 6 to avoid cloud contamination due to the low sun elevation angle (Wuttke et al. 2012). It is thus clear that only a limited amount of data obtained during periods when the sun was obscured by clouds has been taken into account prior to this thesis.

The PFR is still operational and irradiance measurements are available from 2007

to 2014. Additionally, all-sky fish-eye photographs of the cloud situation over Innsbruck have been taken from 2007 to 2014 in an hourly temporal resolution. These photographs are used for a classification of the cloud types. However, this is only possible if the clouds are not too optically thick and allow for transmittance of sufficient radiation which can be measured by the PFR. Therefore, *cloud-contaminated* optical depth measurements (the measurements that were not used by Wuttke et al. 2012) represent measurements of the optical depth (OD) of clouds and aerosols.

The assumptions for deriving AOD from the spectral direct solar irradiance measurements in the algorithm Wuttke et al. (2012) used do not account for clouds. For example, multiple scattering and the strong forward scattering of cloud particles, especially of ice crystals, is not included in the derivation of the OD. Therefore, the cloud-contaminated OD measurements do not reflect all physical processes influencing the measurement.

1.2 Goals and outline

As mentioned above, a large number of the Innsbruck PFR irradiation measurements were never examined, because they were discarded due to the cloud-screening algorithm (see Wuttke et al. 2012). It is conceivable that the same may be valid for many other measurement sites that aim exclusively for AOD examination of cloud-free measurements up to now. Therefore, using cloud-contaminated measurements to infer cloud optical properties would reduce the instruments' idle time. The gathered information would also greatly enhance global coverage of COD measurements and can be used to get *local* estimates for COD (i.e., for a single "sky-element" and not an effective value for the whole visible hemisphere). Therefore, measurements might be used to examine variability of the COD. However, only properties of optically thinner clouds, which are translucent to allow for transmission of enough direct solar radiation (limited by the instrument's sensitivity), can be inferred.

Moreover, hourly all-sky fish-eye images, taken by a camera colocated with the PFR, will be used to determine different cloud types. Hence, optical properties (COD, Ångström exponent α and curvature parameter γ) of different cloud types can be determined. If applicable, these parameters will be used to elucidate the influence of different cloud types on incoming solar radiation. Especially the different influence of high ice clouds and middle to low level clouds (mainly liquid water clouds) will be investigated. Moreover, it might be possible to differentiate cloud types based on the derived properties and use the information for an automatic cloud type detection algorithm.

Hence, the objectives of this work are the following:

(1) Analysis of a cloud-contaminated direct solar irradiance data, measured by a PFR located in the Alpine region.

(2) Calculation of optical properties (COD, α and γ) for optically thin clouds obscuring the sun using AOD information gathered by the same instrument.

(3) Assigning optical properties to different cloud type using all-sky images.

(4) Based on this assignment, compilation of an algorithm to automatically distinguish between cloud types using cloud-contaminated PFR measurements.

The presented thesis is organized as follows: Chapter 2 will introduce the reader to the theoretical background regarding aerosols and radiative as well as optical properties of clouds. In chapter 3, the current state of research for cloud optical depth retrievals using solar radiation in the visible spectral range is presented. Chapter 4 outlines the data and methodology used to derive optical parameters for clouds. Results of this analysis are given in chapter 5. Finally, results are discussed and consequential conclusions are drawn in chapter 6.

2 Physical background

As a foundation for an understanding of the study at hand, the following chapters deal with the basics of radiative transfer in an aerosol-contaminated and cloudy atmosphere. First of all, the properties of aerosols are highlighted, secondly the derivation of the AOD based on Beer's law is shown and, lastly, the radiative properties of clouds are outlined.

2.1 Aerosols

Atmospheric aerosols are compositions of solid and/or liquid particles suspended in the air, excluding hydrometeors like cloud drops, rain, snow or hail. The single particles are called aerosol particles. Aerosol particle size ranges from 10^{-2} to $10^{2}\mu$m (see Fig. 1). Additionally, atmospheric aerosol concentrations and chemical composition exhibit a high variability, depending on, for example, their geographic location. Aerosol sources are either biological, from solid earth, volcanic, anthropogenic or they form in-situ (Wallace and Hobbs 2006).

Biological sources include seeds, pollen, spores and micro organisms like bacteria and fungi. Smoke and ash ejected by forest fires comprise a major part of atmospheric aerosol and play an important role as cloud condensation nuclei. The oceans' surface is a source of salt particles that are transported into the atmosphere by wind and atmospheric turbulence. Sand grains from deserts can be lifted from the surface in the same way (solid earth particles). Aerosol generated by volcanic eruption can sometimes reach heights up to the stratosphere, where the small particles have long enough residence time to be transported globally. Additionally, gases from volcanic origin may condense on existing particles, enhancing their mass, or forming new particles smaller than 0.01 μm. The man-made contribution includes fuel combustion, biomass burning, dust from roads and industrial processes. In summary, the anthropogenic contribution accounts for 20% of the naturally generated aerosol mass. However, it is assumed that by 2040 the number of anthropogenic sources particles could be comparable to the number of natural ones. Sinks of aerosols are liquid and dry fallout, i.e., washout and dry deposition. Scavenging of aerosols via precipitation processes accounts for 80 to 90% of the mass of particles removed from the atmosphere. Growing cloud drops collect very small particles most efficiently. Precipitation washes out especially the particles with diameters around 2 μm by impaction (Wallace and Hobbs 2006).

Aerosol particles are categorized based on on the particle size (see Fig. 1). The very small particles with diameters between 0.001 and 0.2 μm are called Aitken cores. Large particles, or fine/accumulation mode particles, range from 0.2 to 2 μm and even bigger aerosols with diameters D $\gtrsim$ 2 μm are called giant or large particles, or coarse

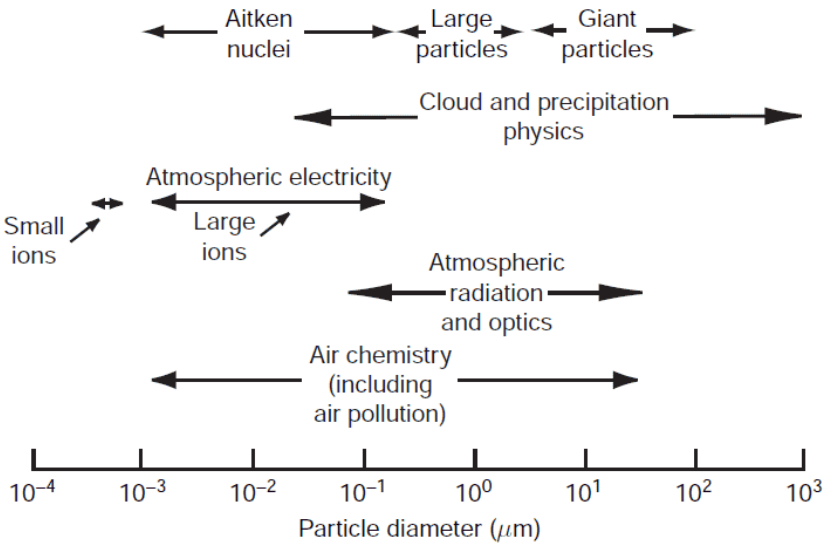

Figure 1: Size ranges of aerosols in the atmosphere and their fields of impact in atmospheric physics. Taken from Wallace and Hobbs (2006).

mode particles. Figure 1 suggests that aerosols of various sizes play an important role in cloud physics. Aerosol particles can serve as cloud condensation nuclei (CCN), depending on their size, solubility and the super saturation in the surrounding air. Generally, bigger and more soluble aerosol particles require a lower supersaturation to serve as CCN (Wallace and Hobbs 2006).

2.2 Aerosol optical depth

In the following chapter the theory of AOD is explained based on Iqbal (1983), Kraus (2004), Wallace and Hobbs (2006) and Wendisch and Yang (2012). Aerosol optical depth is calculated from spectral solar irradiation measurements. The radiation emitted by the sun is attenuated in the earth's atmosphere by absorption and scattering on gas molecules, aerosols and cloud particles. Further, density differences in the atmosphere cause refraction of the sun's beam, as shown in Fig. 2b. For simplification of the complex calculations to account for refraction, most radiative transfer models assume a plane-parallel atmosphere with the optical properties only varying in the vertical direction (see Fig. 2a). The amount of incoming radiation from the sun reaching the top of the atmosphere (TOA) can be calculated straightforwardly from astronomic relationships between sun and earth. The power loss of radiation within the atmosphere is expressed by Bouguer-Lambert's Law, also known as Beer's Law, here in exponential form:

$$I_{\lambda,s} = I_{\lambda,TOA}\, e^{-\int_0^s b_{\lambda,s'}\, ds'}, \tag{1}$$

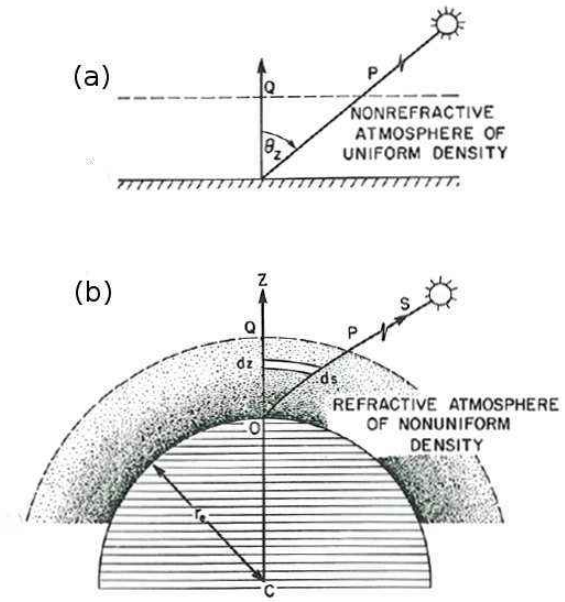

Figure 2: Path of a radiation beam in an (a) plane-parallel non-refractive atmosphere of uniform density and (b) in a curved refractive atmosphere of non-uniform density. In the case of (a) the solar zenith angle is constant, but in (b) it is dependent on the height above the ground due to refraction of the radiation beam. Figure adapted from Iqbal (1983).

where $I_{\lambda,s}$ is the spectral solar irradiance in W m^{-2} at the surface for wavelength λ in m, $I_{\lambda,TOA}$ is the spectral solar irradiation at TOA in W m^{-2}, $b_{\lambda,s'}$ is the spectral volume extinction coefficient in m^{-1}, and ds' is the differential slant path length in m. The PFR measures $I_{\lambda,s}$, the direct beam's irradiance at the ground, and $I_{\lambda,TOA}$ is calculated from astronomical relations. Therefore, the optical attenuation in the atmosphere can now be assessed. To quantify the attenuation of radiation within a medium the concept of the total spectral optical depth $\tau_{\lambda,z}$ can be used:

$$\tau_{\lambda,z} = \int_{z}^{\infty} b_{\lambda,z'}\, dz', \tag{2}$$

which is dimensionless. The optical depth is zero at TOA and increases towards the surface where it becomes $\tau_{\lambda,0} = \int_{0}^{\infty} b_{\lambda,z'}\, dz'$. In the plane-parallel atmosphere the slant path length ds, inclined to the zenith with the solar zenith angle θ (illustrated in Fig. 2a, there θ_z), is $ds = \frac{dz}{cos\theta}$. Using this relation and the optical depth $\tau_{\lambda,z}$ as vertical coordinate, Eq. (1) simplifies to

$$I_{\lambda,z} = I_{\lambda,TOA} e^{-\tau_{\lambda,z}\frac{1}{cos\theta}}, \tag{3}$$

whereas the fraction in the exponential is also termed relative optical airmass $m_{rel} = \frac{1}{cos\theta}$. It describes the dependency of the radiation extinction on zenith angles and is, in this form, only valid in a plane-parallel and non-refractive atmosphere.

The total optical depth $\tau_{\lambda,z}$ is composed of the optical depths of the single constituents of the atmosphere, for instance, ozone (O_3), nitrogen dioxide (NO_2), aerosols and air molecules. The attenuations by the single constituents add up to the total dilution of solar radiation:

$$\tau_{\lambda,z}\ m_{rel} = \sum(\tau_{\lambda,z,i}\ m_{rel,i}). \tag{4}$$

In the plane-parallel atmosphere m_{rel} the relative optical airmass is the same for all constituents, as it depends only on the zenith angle θ. However, for a more realistic approach the relative optical airmass for every constituent can be calculated using assumptions on the atmospheric component's vertical distribution, for example from the Standard Atmosphere. There are also empirical approaches (as from Kasten 1965; Kasten and Young 1989; Komhyr et al. 1989), of which some were used in this work (see chapter 4.2.1). The sun's beam is attenuated by the aforementioned atmospheric constituents and other influences. In the visible range of the electromagnetic spectrum the most important contributions to extinction are from NO_2, O_3, aerosols and Rayleigh scattering (see chapter 2.3). Other atmospheric gases' (like water vapor) absorption bands do not coincide with the wavelengths of the PFR and are, therefore, not taken into account.

The AOD can be inferred if the TOA radiation, the amount, distribution and type of atmospheric constituents and the incoming direct beam solar irradiation at the ground level are known either from measurements or by using approximations. The incoming solar radiation at TOA and the distribution of NO_2 and O_3 in the atmosphere are only estimates, however, the values are known very well. Therefore, the attenuation by aerosol, i.e. the spectral AOD $\tau_{\lambda,a}$, can be computed if several parameters are known: the incoming radiation at the ground, $I_{\lambda,z}$, the radiation at the TOA, $I_{\lambda,TOA}$, the total optical depths, $\tau_{\lambda,z,i}$, and optical airmasses, $m_{rel,i}$, of several atmospheric constituents affecting radiation. In the following approach, only Rayleigh scattering and extinction by O_3 and NO_2 are taken into account:

$$\tau_{\lambda,z,a} = \frac{1}{m_{rel,a}}(ln\big(\frac{I_{\lambda,z}}{I_{\lambda,TOA}}\big) + \tau_{\lambda,z,R}\ m_{rel,R} + \tau_{\lambda,z,O_3}\ m_{rel,O_3} + \tau_{\lambda,z,NO_2}\ m_{rel,NO_2}). \tag{5}$$

The calculated optical depth is the remainder term after subtracting the most important physically reasonable attenuator contributions from the signal at the ground. This remainder is assigned to the AOD. In a further step the AOD can be used to deduce information of the particle size distribution of the aerosol.

Particles of various sizes attenuate radiation in a different way depending on the wavelength. Spectral AOD variations can be used to derive information about the aerosol size distribution (Kaufman 1993). Angström (1929) found an empirical formula, called Ångström's turbidity formula, for the aerosol spectral behavior:

$$\tau_{\lambda,a} = \beta\ \lambda^{-\alpha}. \tag{6}$$

The wavelength λ is here used in μm, α is the Ångström exponent which describes the size of the aerosol particles and β, the turbidity coefficient, represents the AOD $\tau_{\lambda,a}$ for $\lambda = 1\mu$m. However, the values of the Ångström coefficients do not have a direct physical meaning (in contrast to the AOD) but can be used for empiricism based conclusions.

Large values of α imply a strong wavelength dependence of the AOD. Therefore, when α exceeds one mainly fine mode aerosols with radii smaller than 1 μm are present in the atmosphere. For values of α below one, indicating a lower wavelength dependence, coarse mode aerosol dominate the size distribution with radii above 1 μm. When α approaches zero, wavelength dependence decreases and vanishes with $\alpha = 0$. This implies that, in addition, Mie scattering (see chapter 2.3) has to be taken into account. In summary, the range of α spans from zero for large particles to four for air molecules.

Beside deriving particle size, the Ångström exponent can be used for extrapolating AOD throughout the shortwave spectral region (Schuster et al. 2006). After using the natural logarithm on Eq. (6) it can be written as a linear correlation between $ln\tau_{\lambda,a}$ and $ln\lambda$:

$$ln\tau_{\lambda,a} = ln\beta - \alpha\ ln\lambda. \tag{7}$$

The Ångström exponent α can be interpreted as the negative slope of the linear correlation and $ln\beta$ as its axis intercept. Both parameters can be derived from a linear regression of AODs and corresponding wavelengths, as further described in chapter 4.2. However, it is important to notice that the value of α is not constant but depends on the set of wavelengths which are used for its calculation. Therefore, Angström (1964) introduced a more precise approach with an additional second-order term

$$ln\tau_{\lambda,a} = ln\beta^* + \alpha^*\ ln\lambda + \gamma\ (ln\lambda)^2, \tag{8}$$

where γ accounts for the curvature of the correlation curve. If the third Ångström parameter γ is negative, the aerosol size distribution has a large fraction of fine mode aerosol, and when it is positive, the distribution is dominated by coarse mode aerosol (Wuttke et al. 2012; Schuster et al. 2006; Eck et al. 1999).

2.3 Radiative and optical properties of clouds

A cloud is an aggregate of liquid cloud drops or ice crystals or a combination of both (mixed-phase cloud). For a cloud to be visible, the cloud particles must be present in a sufficiently large concentration. This definition originates from operational weather forecasting which quantifies cloud coverage as a fraction of cloudy sky relative to the visible hemisphere. The cloud coverage fraction is given in eights. Beside that more subjective and operational approach, the presence of a cloud can be characterized by its cloud optical depth (Lohmann et al. 2016).

The optical depth of a cloud depends on microphysical properties like the particle size distribution, the number density of cloud hydrometeors and the phase of the parti-

Table 1: Typical values and ranges of cloud particle sizes in μm, according to Lohmann et al. (2016). The size values of liquid cloud hydrometeors refer to the radii of the drops, whereas the size values of ice cloud particles refer to the maximum dimension of the crystals due to their nonsphericity.

	typical size	range
Cu	6	2 - 25
Sc, St	4	2 - 12.5
Ac, As	4	2 - 10
Ci, Cs, Cc	100	1 - 1500

cles. Low-level clouds consist mainly of liquid hydrometeors while high-level clouds are made up of ice crystals. However, also mixed-phase clouds consisting of liquid and solid hydrometeors exist, mostly in mid-tropospheric levels. Table 1 lists the typical sizes and possible size ranges of cloud particles according to Lohmann et al. (2016) for different cloud types. Low Stratocumulus (Sc) and Stratus (St) and mid-level Altocumulus (Ac) and Altostratus (As) exhibit the same mean particle radius (4 μm) and a similar radius range (2 - 10 μm, respectively, 2 - 12.5 μm). Cumulus (Cu) clouds show slightly larger typical radii (6 μm) and a considerably larger size range (2 - 25 μm). Even larger is the typical ice crystal of high-tropospheric clouds like Cirrus (Ci), Cirrostratus (Cs) and Cirrocumulus (Cc) clouds (100 μm radius) with a particle size distribution ranging from 1 to 1500 μm. Figure 3 exemplarily shows the number size distribution of a Cirrus cloud, derived from airborne in-situ measurements, which are in good agreement with the values given in table 1.

Nevertheless, the specific crystal size distribution within an ice cloud is dependent on the temperature and humidity conditions within the cloud. Additionally, the ice crystal morphology strongly depends on these conditions. Altogether, radiative properties of ice clouds are heavily influenced by crystal size and shape. However, not only cloud types differ from each other, even within one cloud a wide variety of crystal morphologies can be present.

The most obvious effects of clouds are scattering and absorption of solar radiation. Solar radiation is scattered and absorbed in the atmosphere by air molecules, aerosols and cloud particles. Scattering processes affect the whole electromagnetic spectrum but are wavelength dependent.

Many theoretical approaches consider single scattering processes (when radiation interacts with only one molecule or particle). However, in reality multiple scattering occurs (radiation interacts with a number of particles or molecules). Single scattering processes are mostly taken into account in simplified approaches and theoretical frameworks. Scattering does not influence the amount of energy transported by the radiation. Besides scattering, clouds absorb radiative energy and transform it into internal energy. Therefore, it is not longer available as radiant energy of its original

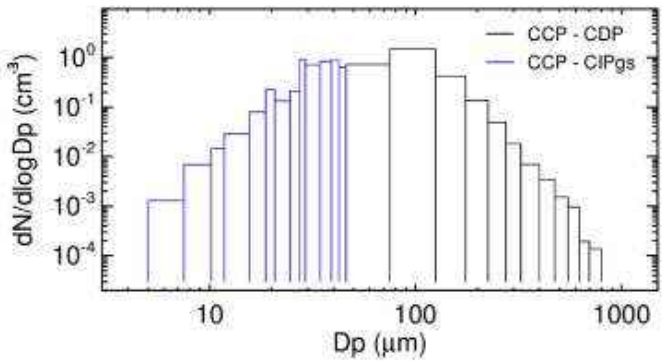

Figure 3: Number size distribution of a Cirrus cloud's ice crystals, measured in-situ by a cloud contamination probe (CCP). The CCP consists of the cloud droplet probe (CDP) for detection of particles with diameters Dp from 2 to 50μ and the cloud imaging probe (CIP) for detection of particles with diameters from 15 to 960μ. The ordinate displays the change of particle number density N per logarithmed change of Dp in cm^{-3} (taken from Finger et al. 2016).

wavelength. The efficiency of absorption is dependent on the imaginary part of the refractive index of the absorbing material (Boucher 2015).

Figure 4b shows that the imaginary parts of the refractive index for water and ice in the VIS are very much alike. The spectral variability, which is responsible for the level of absorption of solar radiation by clouds, is high: it ranges from 10^{-10} to 10^{-6} for a wavelengths range from 0.5 to 1 μm. Therefore, in the VIS range longer wavelengths are absorbed more strongly. However, the real part of the refractive index determines, amongst other parameters, the scattering efficiency. Figure 4a reveals slightly decreasing real parts of the refractive index for increasing wavelength for both water and ice, with a slightly higher absolute value for water throughout the given wavelength range (Kokhanovsky 2004; Boucher 2015; Lohmann et al. 2016).

Scattering in a gaseous medium can be described on the molecular scale. Scattering occurs if the wavelength of the incident photon does not coincide with the molecule's absorption bands. The amount of the incoming radiant energy, and, in turn, the wavelength, remain unchanged. However, the direction of the incoming radiation is altered during scattering processes. For solar radiation that means *direct* radiation is transformed into *diffuse* radiation.

Especially within clouds, when a large number of particles, i.e. cloud hydrometeors, are present a huge number of interactions between the radiation and the particles occurs. Therefore, the medium (for example, the cloud) has to be described on the macroscopic scale considering a distribution of particles, and taking into account their shape (spherical or not), their size distribution and their refractive index. With these parameters the scattering properties can be modeled according to the Mie theory (see below) (Boucher 2015; Lohmann et al. 2016).

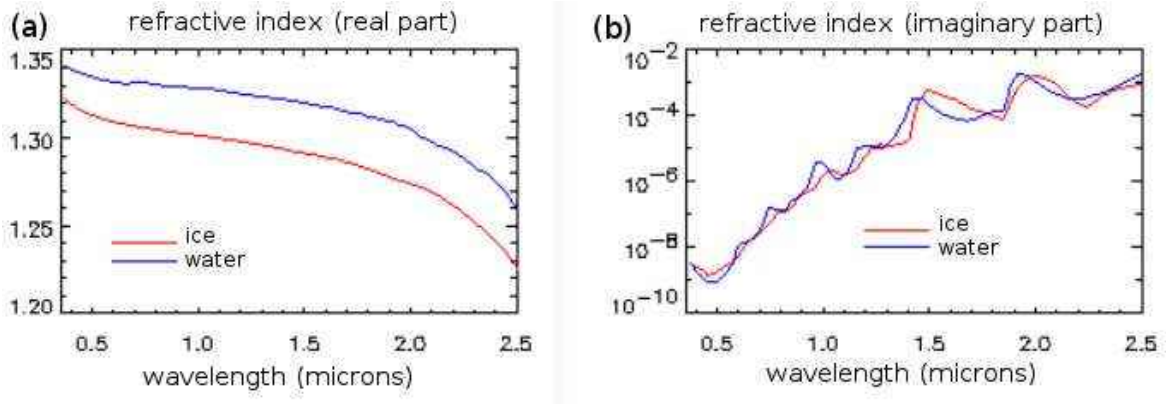

Figure 4: Refraction index of water (blue) and ice (red). In (a) the real part of the refractive index is shown which determines, amongst other parameters, the scattering efficiency. The real parts of the refractive index for water and ice do not change considerably in the VIS region of the spectrum, whereas the imaginary parts in (b) both for water and ice vary by about three orders of magnitude with lower values for shorter wavelengths. The imaginary part of the refractive index is connected to the absorption efficiency (Randall P. Julander cited 2016)

.

The scattering regime depends on the size of the scattering particle and the wavelength of the incoming radiation. The relationship between the particle radius r and the wavelength λ is expressed by the dimensionless size parameter χ:

$$\chi = \frac{2\pi\ r}{\lambda}. \tag{9}$$

Figure 5 illustrates this dependence and shows the possible scattering regimes. Due to the many different particle sizes and the presence of several atmospheric constituents all regimes occur under realistic conditions in the atmosphere for the visible spectrum of solar radiation. These scattering regimes are:

Rayleigh scattering $\chi \ll 1$

According to Rayleigh's theory for very small particles (for instance, molecules) compared to the incident wavelength the optical depth due to scattering τ_R, also called Rayleigh optical depth, is

$$\tau_R \propto \lambda^{-4}, \tag{10}$$

with the wavelength λ given in μm (Boucher 2015). This strong wavelength dependence of λ^{-4} causes much more intense scattering for shorter wavelengths. Therefore, in the VIS region of the spectrum molecules scatter particularly shorter wavelengths (blue), causing the color of the sky. The angular distribution of light intensity scattered by a particle at a given wavelength is described by the scattering phase function. In the case of Rayleigh scattering forward and backward scattering are of the same intensity, while scattering to the sides has approximately half of the forward scattered intensity. In Fig. 6 the normalized phase function is depicted for an molecule hit by radiation

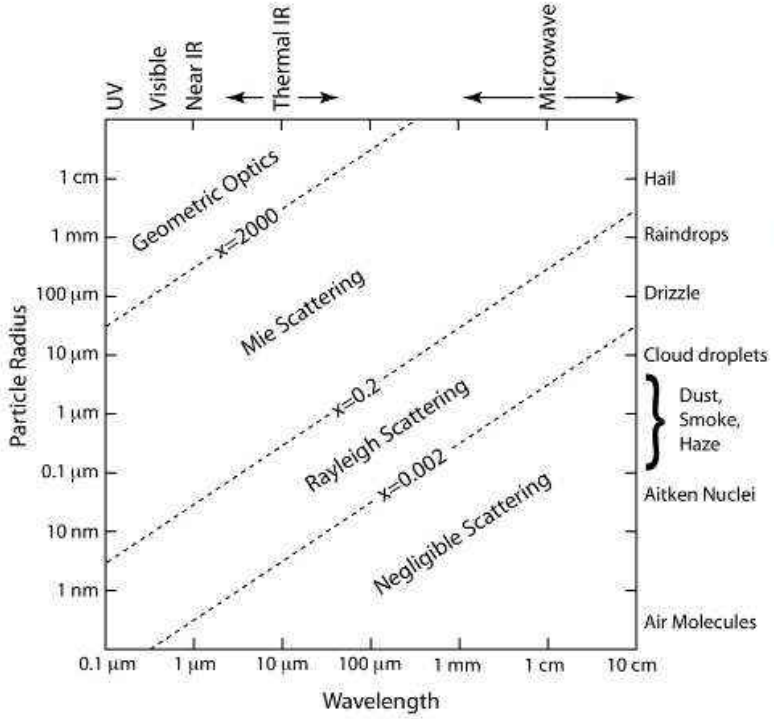

Figure 5: Scattering regimes depending on wavelength of the incoming radiation and particle radius of the scatterer. The transition values of the scattering regimes are marked in the figure by dotted lines with the corresponding size parameter χ. On the top the ranges of the electromagnetic spectrum are labeled and on the right molecules, aerosols and hydrometeors are assigned to their typical particle radius (taken from Boucher 2015).

with $\lambda = 500$ nm (Liou 2002; Boucher 2015).

Mie scattering $\chi \gtrsim 1$

For larger particles like aerosols or cloud drops and wavelengths in the visible spectrum the Rayleigh theory is not valid anymore. If wavelength and particle radius have approximately the same value, i.e. $\chi \approx 1$, Mie scattering dominates. The wavelength dependence in the Mie scattering regime is small. According to the Mie theory, optical properties of a particle depend only on the size parameter χ and the particle's refractive index m. According to the Mie theory the scattering efficiency Q_{sca} is:

$$Q_{sca} = \frac{s_{sca}}{s_g}, \tag{11}$$

with s_{sca}, the scattering cross section, and s_g, the geometrical cross section, in m^2. The former is defined by

$$s_{sca}(\lambda) = \frac{24\pi^3}{N^2\lambda^4}\frac{(m^2-1)^2}{(m^2+1)^2}, \tag{12}$$

where N is the number density of the particles in m^{-3} and m the refraction index of the particle (Boucher 2015). For a non-absorbing spherical particle with a refractive index of $m = m_r + i\ m_i = 1.33$ the extinction efficiency is depicted in Fig. 7. The real part

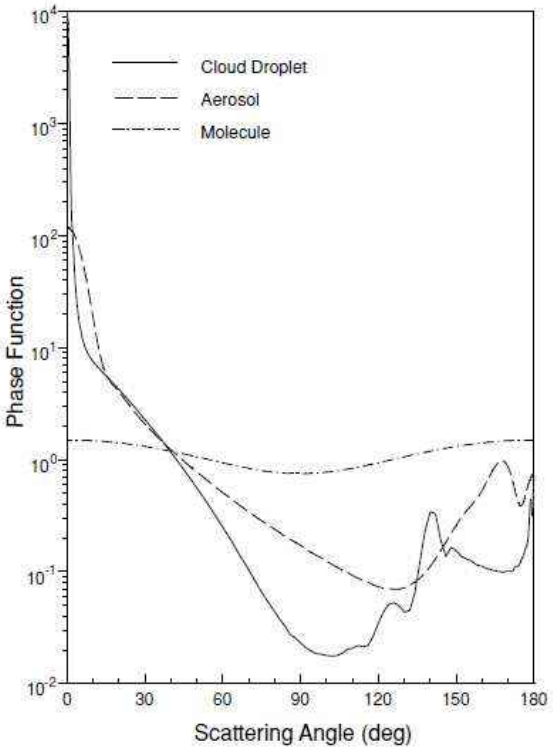

Figure 6: Normalized scattering phase functions according to Liou (2002): for cloud droplets (approximately 10 μm), aerosols (approximately 1 μm), and molecules (approximately 1 to 4 Å) during interacting with radiation with a wavelength of 0.5 μm, based on Mie theory.

of the refractive index m_r describes the scattering behavior, while the imaginary part m_i accounts for absorption. This scattering behavior is representative for water, that exhibits a $m_r \approx 1.33$ in the VIS part of the spectrum ($m_r \approx 1.31$ for ice). The m_i of water and ice ranges from 10^{-10} to 10^{-7} for the wavelengths used for the measurements presented in this thesis (368, 412, 501 and 861 nm). The absorption efficiency is negligibly small compared to the scattering efficiency (Petty 2006). Therefore, in the following instead of extinction efficiency the term scattering efficiency is used. For very small size parameters the scattering efficiency is proportional to χ^4, resp. λ^{-4}, as in the aforementioned Rayleigh regime. For large size parameters the scattering efficiency approaches two (see Fig. 7a). Size parameters in between exhibit resonance phenomena which can reach scattering efficiencies of up to four, as illustrated in Fig. 7a. Figure 7b shows high-frequency fluctuations inherent to the Mie scattering efficiency depending on the size parameter in more detail. Assuming a constant particle radius r, for $\chi \lesssim 6$ shorter wavelengths are scattered more intensely than longer wavelengths. In the VIS part of the spectrum this results in a reddening of the radiation. This effect is responsible for the orange-reddish sun at dusk. If the particle size is somewhat larger the opposite can be the case: longer wavelengths are scattered more, yielding blueing. This configuration of particle sizes and wavelengths with χ between six and eleven

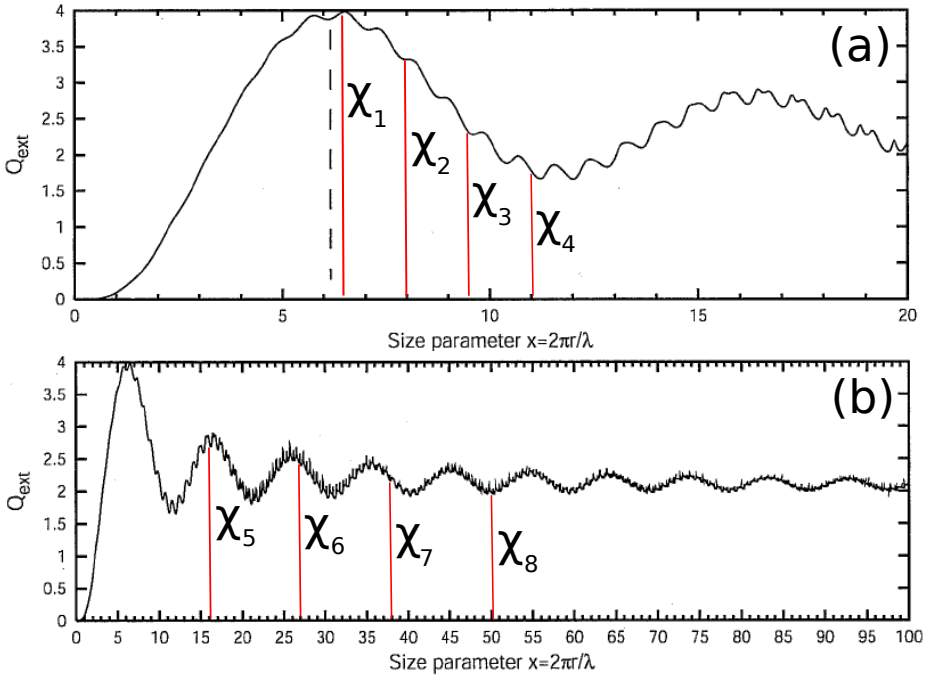

Figure 7: Extinction efficiency calculated according to the Mie theory for a particle with a refraction index of $m = 1.33$ (like water), presented in relation to the size parameter $\chi = \frac{2\pi r}{\lambda}$ (taken and adapted from Petty 2006). Panel (a) shows the fluctuating scattering efficiency for χ from zero to 100 with relative maxima and minima for distinct size parameters. For χ tending towards $+\infty$ the scattering efficiency tends to two. The concept of reddening and blueing is pictured in (b). For a fixed particle radius and, for example, in the range of zero to six a higher χ yields more scattering for shorter wavelengths resulting in reddening. In the χ range from six to eleven it is the other way around, resulting in blueing of the radiation. In chapter 5.1 the extinction efficiencies marked red will be highlighted. (a) *Decreasing* extinction efficiency for slightly *increasing* size parameters χ_1 to χ_4, calculated using a fixed particle size r and *decreasing* wavelengths $\lambda_1 > \lambda_2 > \lambda_3 > \lambda_4$. (b) *Decreasing* extinction efficiency for *increasing* size parameters χ_5 to χ_8, calculated using a fixed particle size r and *decreasing* wavelengths $\lambda_5 > \lambda_6 > \lambda_7 > \lambda_8$ (taken and adapted from Petty 2006).

is rare in the atmosphere (Kraus 2004; Petty 2006). However, in 1950 a "blue sun" could be observed in the northern hemisphere because smoke aerosol from forest fires in Canada was advected around the globe (Kraus 2004). This specific aerosol caused larger scattering efficiency for the longer solar wavelengths and, therefore, exhibited a negative Ångström α. Figure 5 shows that scattering in clouds is subject to the Mie theory, as well as geometric optics, which are described in the following section (Liou 2002; Boucher 2015).

Moreover, Mie scattering exhibits very strong forward scattering. As an example, in Fig. 6 the phase functions of an aerosol and a cloud drop for a wavelength of 500 nm are shown. The intensity in the forward direction is two and more magnitudes higher than for Rayleigh scattering (Liou 2002). Ice crystals forward scattering is even stronger than forward scattering on cloud drops (Min et al. 2004).

Geometric optics $\chi \gg 1$

The optical properties of particle-radiation interactions with χ clearly exceeding one are explained by geometrical optics. In this case, the geometric ray-tracing method can be applied: a light beam can be thought of as consisting of a bundle of separate parallel rays that hit the particle or go around it (for more detail see Fu 1996). The rays impinging on the scatterer will undergo reflection and refraction, the ones that pass around experience diffraction. Diffraction on, for example, liquid cloud droplets can cause the optical phenomenon of a corona. For a corona shorter wavelengths are deflected stronger around the drop, resulting in a colored ring around the sun with blue inside and red color on the outer side of the ring. Refraction causes a change of direction for the incoming ray when entering and leaving a particle like a liquid water drop. The dependence of the angular deviation is given by Snell's law:

$$\frac{sin\theta_1}{sin\theta_2} = \frac{m_2}{m_1}, \tag{13}$$

where θ_1 is the angle of incidence of the ray, θ_2 the refracted angle, m_1 the refraction index of the first medium and m_2 of the second. A combination of refraction and reflection of sunlight in water droplets cause the formation of rainbows. However, halos are caused by solar ray refraction in ice crystals that have a known specific form and orientation (Boucher 2015).

Methods for nonspherical objects in the Mie range

However, other methods are required if a particle is nonspherical or nonhomogeneous and its size is similar to or larger than the incident wavelength, i.e. $\chi \gtrsim 1$ (like ice crystals in the visible spectral range). The Anomalous Diffraction Theory, for example, assumes that extinction is largely caused by absorption of the radiation, as well as by the interference of light beams passing through the particle and light beams passing around by diffraction. Refraction and reflection are neglected. The approach can be applied to nonspherical particles, such as spheroids and hexagons, but when used for ice crystals the accuracy can decrease by neglecting refraction and reflection (for further reading see Liou 2002). Another technique has been described by Grenfell and Warren (1999). Their approach was to resemble several ice crystal morphologies by using a collection of individual small ice spheres. The ice spheres alltogether exhibit the same total mass, total surface area and total volume as the specific crystals. Scattering properties were then calculated using the Mie theory. The ice crystals were approximated by infinite circular ice columns, to enable an exact solution of the Maxwell equations. The Mie calculations with the collection of spheres yielded good agreement for the extinction efficiency and phase function, for instance.

As mentioned above, table 1 lists the typical particle radii for different cloud

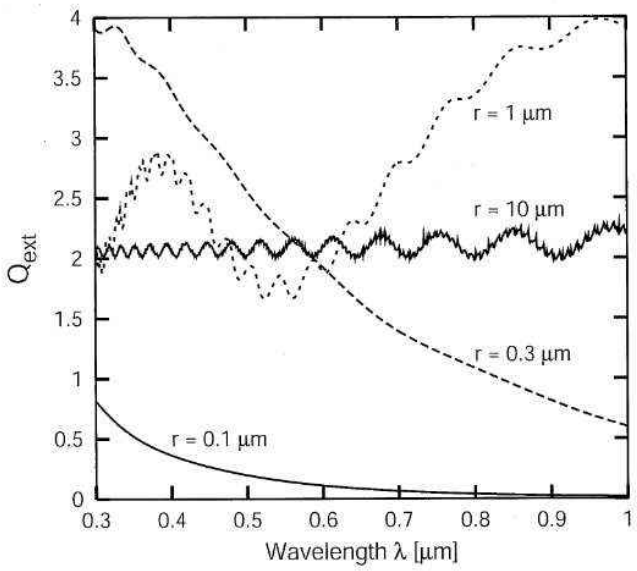

Figure 8: Extinction efficiency calculated according to the Mie theory for a particle with a refraction index of m=1.33 (like the real part of the refraction index of water), presented in relation to wavelength for various particle radii (taken from Petty 2006).

types. A typical spherical cloud drop radius of 4 μm and the wavelengths 368, 412, 501 and 861 nm of the measuring instrument yield size parameters between 30 and 70. These values are in a χ-range where the scattering efficiency still varies strongly (see Fig. 7). In contrast, Fig 8 illustrates the dependence of the scattering efficiency on the wavelength (instead of size parameter as in Fig. 7) for various particle radii. For cloud particles with radii from 1 to about 10 μm the scattering efficiency in the VIS varies stronger for smaller cloud drops. For example, a particle with a radius of 1 μm exhibits scattering efficiencies of roughly 2.5, 2.5, 2 and 3.5 for the wavelengths 368, 412, 501 and 861 nm. This spectral enhancement of extinction indicates an increasing COD with wavelength. This positive relation of λ and COD yields a negative Ångström exponent α (see chapter 4.2.1). Negative α are not present in the Rayleigh scattering regime but can occur for Mie scattering and probably also for geometric optics scattering in ice crystals, as presented in chapter 5.

3 State of research

A wide variety of peer-reviewed literature exists about cloud radiative properties, their derivation using a multitude of different techniques and their influence on climate. Therefore, this chapter will focus on ground-based retrieval algorithms of cloud optical depth, comparable to the one used in this thesis.

Marshak et al. (2000) proposed an approach using zenith radiance measurements in the red and near-infrared (NIR) spectral regions to derive a non-dimensional cloud index. Their approach is based on the fundamentally different radiative behavior of green vegetation and liquid cloud drops in the red and NIR spectral regions: Cloud reflectivity shows little difference between these two spectral regions. In contrast, vegetation albedo is low (high) for incoming radiation in the red (NIR) spectral region. In other words, vegetation reflects much more radiation in the NIR than in the red spectral region and "illuminates" clouds in the NIR spectral region from below. Additionally, optically thick clouds exhibit a higher cloud-base reflectance of the surface-reflected NIR radiation than optically thin clouds. Therefore, ground based upward pointing (zenith) measurements of cloud-base reflected radiance in these specific spectral regions show a strong (low) spectral contrast under optically thick (thin) clouds. Marshak et al. (2000) use this behavior to compile a spectral index, called Normalized Difference Cloud Index (NDCI)

$$NDCI = \frac{I^{\downarrow}(VIS) - I^{\downarrow}(NIR)}{I^{\downarrow}(VIS) + I^{\downarrow}(NIR)}. \tag{14}$$

Following their approach, the NDCI is negative for clear-sky conditions and positive for an overcast sky. However, during broken cloud conditions the NDCI is ambiguous and can have either a positive or a negative value, depending on the presence of a cloud in the zenith direction of the instrument (Davis and Marshak 2010). A benefit of the described approach is that a one-dimensional radiative transfer model can be used even under broken cloud conditions which would usually only produce valid results for overcast conditions (Marshak et al. 2000). Additionally, inferring NDCI is nearly insensitive to the SZA (Marshak et al. 2004) whereas large SZAs impose problems to several retrieval techniques to infer COD.

Barker and Marshak (2001) extended the approach of Marshak et al. (2000) to derive COD information instead of the NDCI. They found that two simultaneous measurements in different spectral regions are necessary because zenith radiances lack a direct one-to-one relationship to infer COD (see Fig. 1 in Barker and Marshak 2001, or Fig. 9 herein, taken from Chiu et al. 2007). Additionally, Barker and Marshak (2001) proved that the proposed approach can be used above all surfaces which ex-

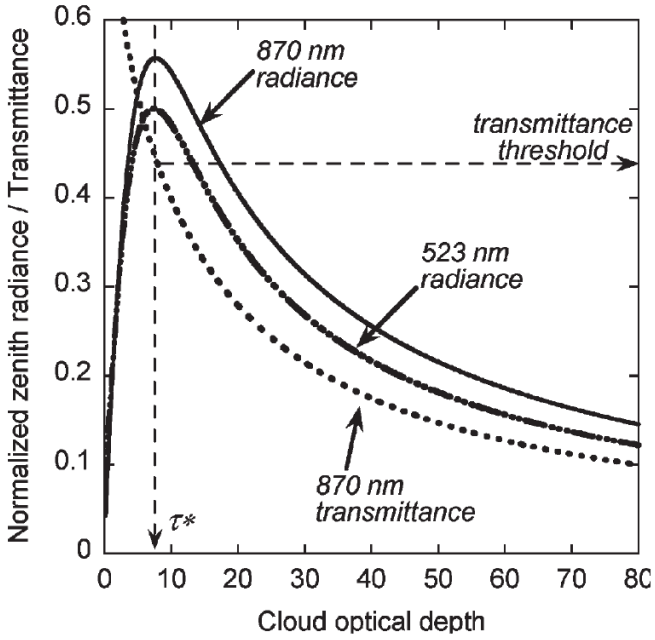

Figure 9: Downward zenith radiance at 523 and 870 nm and transmittance at 870 nm as a function of cloud optical depth. Curves are calculated by using a one-dimensional radiative transfer model for a solar zenith angle of 60°. The transmittance threshold associated with maximum zenith radiances is indicated. Figure is taken from Chiu et al. (2007) and details can be found therein.

hibit a difference in spectral surface albedo higher than 0.1 and is not limited to green vegetation areas only. Finally, Marshak et al. (2004) used the spectral NDCI approach to derive COD information during broken cloud conditions. Their approach used zenith radiance measurements in the red and NIR spectral regions gathered by a multichannel Sun photometer of the AERONET network. These instruments were initially intended to gather AOD measurements (see chapters 4.1 and 4.1.2). Marshak et al. (2004) proposes to use the present instrumentation at AERONET sites to derive COD information during conditions which are not suitable to derive AOD information (for example, when clouds obscure the Sun and AOD retrievals are not possible) to reduce the instrument's idle time. Using instrumentation of an operational network like AERONET can provide a high global coverage of measurements if the COD derivation technique is applied globally. However, knowledge of the surface albedo and its heterogeneity around measurement sites is essential to derive reasonable COD values since the retrieval approach of Marshak et al. (2004) relies on surface-cloud interactions. Marshak et al. (2004) validated COD values derived by using the spectral difference approach with other COD estimations, calculated by using a multifilter rotating shadowband radiometer (MFRSR) and a microwave radiometer. They found that their approach agrees well with other measurement techniques. Additionally, the algorithm developed by Marshak et al. (2004) derives a radiatively effective cloud fraction that takes the cloud internal structure into account. This is achieved by fitting derivations

of the radiatively effective cloud fraction to one-dimensional radiative transfer calculations. The effective cloud fraction can provide information on the degree of cloud inhomogeneity (Marshak et al. 2004).

Beside AERONET instrumentation, observation sites of the Atmospheric Radiation Measurement (ARM) Program (Shupe et al. 2016) have been extensively used to derive cloud properties. ARM sites are equipped with a multitude of active and passive instruments and, therefore, allow for retrieval techniques which combine several sensors to retrieve cloud properties. Several COD retrievals using instrumentation of the ARM Program have been developed. For example, the above mentioned approach of Marshak et al. (2004) is also applicable to ARM sites, as the instrumentation includes the same type of Sun photometer as the AERONET setup. Chiu et al. (2007) used a two-channel Sun photometer of the ARM Program, operating at 673 and 870 nm wavelength, to derive COD information using the same approach as Marshak et al. (2004). Beside that, Chiu et al. (2007) also derived COD information using a single-channel Sun photometer operating at 870 nm measuring zenith radiances. As a one-to-one relation between zenith radiance and COD is missing, i.e. a single zenith radiance measurement can be associated with both optically thin and optically thick clouds (as mentioned above and shown in Fig. 9), additional information is necessary for a final retrieval. Chiu et al. (2007) calculated cloud transmittance for the 870 nm wavelength using collocated MFRSR measurements. Cloud transmittance associated with maximum values of zenith radiance is used as a threshold (see Fig. 9). However, this transmittance threshold is not constant but dependent on the SZA (Chiu et al. 2007). When measuring zenith radiance, the simultaneously inferred transmittance is used to determine if the zenith radiance is associated with low or high COD values. When the inferred transmittance is smaller (greater) than the transmittance threshold the higher (lower) COD value is assigned to the measurement.

Chiu et al. (2007) also proposed a sophisticated approach using a micropulse lidar (MPL) system operating at a wavelength of 523 nm in their study to derive COD information. Additionally, they compared MPL-derived COD information to the retrievals using a Sun photometer, as described above. During MPL measurements, solar radiation, which is gathered in addition to the backscattered laser emitted by the lidar, is considered signal noise. This *solar signal noise* is especially evident near solar noon or when bright clouds are in the FOV of the lidar. However, the contribution of the solar radiation can be estimated during measurements (for details see Chiu et al. 2007). Therefore, for vertically pointing MPL measurements the solar background noise can be interpreted as the solar zenith radiance, which in turn can be used to derive cloud optical properties. However, MPLs need to be calibrated in laboratory or with collocated Sun photometer measurements in order to implement the proposed measurement technique (Chiu et al. 2007). Single zenith radiance measurements cannot be used to

derive COD unambiguously, due to the relation between solar zenith radiance and COD depicted in Fig. 9. In order to distinguish between optically thick and optically thin clouds Chiu et al. (2007) used the attenuation of the lidar beam. They assumed that, if the lidar beam is completely attenuated during a measurement, optically thick clouds are present and, therefore, the higher COD values is assigned to the measurement, and vice versa.

Retrieval errors of the solar background MPL approach are around 10 to 15% when compared to COD retrievals using Sun photometers (Chiu et al. 2007). The approach using solar background radiation eliminates the constraint that direct measurements of COD, using lidar signal backscatter, are limited to cloud situations with $\tau < 3$ due to low lidar returns for higher CODs (i.e., high attenuation by clouds). However, the ambiguous COD retrieval shown in Fig. 9 can result in situations when it is hard to decide whether the higher or lower COD values are valid for a single measurement. This is especially evident for the COD range from 3 to 15 (Chiu et al. 2007). Therefore, additional information is required in this specific COD range, which is a drawback of the proposed approach. Additionally, MPLs are not as widely used as Sun photometers and are more expensive in maintenance and acquisition. On the other hand, Chiu et al. (2007) mention that MPLs are capable of deriving aerosol properties during clear-sky conditions via lidar signals and COD information of optically thick clouds during cloudy periods via solar background lights. This is a capability, which few ground- or satellite-based instrument share. However, the approach of Min et al. (2004) described below is also capable of retrieving both, aerosol and cloud information, while using a single MFRSR.

All of the above mentioned retrieval techniques rely on the solar zenith radiances, i.e., diffuse radiation measurements, to retrieve the optical properties of clouds. However, for optically thin clouds, which produce inhomogeneous scattering (such as boundary layer Cumulus, Cirrus or Cirrostratus clouds), these approaches are not applicable (Min et al. 2004). Therefore, another approach to derive COD information of optically thin clouds is used to infer transmittances for direct solar beam radiation by relying on Beer's law (see Eq. 1; Min et al. 2004). A similar approach is also used in the presented thesis (see chapter 4). Nevertheless, direct solar beam measurements are contaminated by i) forward scattering of radiation into the instrument's FOV (especially evident for cirrus clouds due to strong forward scattering by ice crystals) and ii) extinction by the presence of aerosols (Min et al. 2004). The former results in an underestimation of the derived cloud optical depth, while the latter results in an overestimation if the influence of aerosols is not taken into account. Min et al. (2004) approximate optical depth due to Rayleigh scattering, as well as gaseous absorption (mostly ozone) as constant values and remove that influence from the *apparent* (i.e., measured) optical depth. Further, the influence of aerosols on optical depth is determined. First of all, the wavelength

dependence of the COD within the VIS spectrum is rather low and, therefore, a linear relationship between the COD at 415 nm (τ_c^{415}) and 860 nm (τ_c^{860}) is assumed

$$\tau_c^{415} = \sigma \tau_c^{860} \tag{15}$$

with $\sigma = 0.989$ (0.968) for water (ice) clouds (Hu and Stamnes 1993; Fu 1996).

After eliminating the influence of gaseous extinction and Rayleigh scattering, as mentioned above, Min et al. (2004) assume that the apparent optical depth at wavelengths of 415 and 860 nm (τ^{415}, resp. τ^{860}) can be described with

$$\tau^{415} = \beta \; 0.415^{-\alpha} + \tau_c^{415} \tag{16}$$

and

$$\tau^{860} = \beta \; 0.860^{-\alpha} + \tau_c^{415}\sigma^{-1} \tag{17}$$

while using the linear relationship of Eq. 15.

Min et al. (2004) use an approach to determine the influence of aerosols on the optical depth based on the different temporal and spectral characteristics of aerosols and clouds. Aerosol properties can only be inferred with direct solar beam measurements during clear-sky conditions. During cloud situations characterized by optically thin, broken clouds, the temporal scale of the presence of thin clouds within the instruments FOV is on the order of minutes (i.e., clear-sky and cloud contaminated measurements alternate temporally). On the other hand, the particle size distribution of aerosol (i.e., Ångström exponent α) changes in the order of hours to days. In the same way, β, which is related to the extent of aerosol loading in the atmosphere, has a temporal scale in the order of hours (Min et al. 2004). Therefore, it is possible to use a constant value for α in Eqs. 16 and 17.

In order to infer a numerical value for α, Min et al. (2004) developed an approach using a threshold value α_{thre}: If the maximum value of α exceeds 1 for a given day, α_{thre} is set to 80% of that maximum value, otherwise $\alpha_{thre} = 0.8$ is used (a typical value for continental aerosol in winter according to Michalsky et al. 2001). In turn, α_{thre} is used to distinguish between clear-sky and cloud contaminated situations. When α, inferred from single spectral MFRSR measurements at 415, respectively, 860 nm, on a given day is higher (lower) than α_{thre}, clear-sky (cloud contaminated) conditions are assumed. This is based on the empirical relationship of Ångström's turbidity formula (Eq. 6), which relates bigger particles (i.e., aerosols or even bigger cloud particles) to lower values of α and higher values of α to molecular scattering (i.e., clear-sky conditions). During cloud-contaminated conditions, α is assumed to be constant and set to the same numerical value as α_{thre}. This allows the use of Eqs. 16 and 17 to infer COD information. With the optical depths τ^{415}, resp. τ^{860}, derived from MFRSR measurements, and $\alpha = \alpha_{thre}$, β and τ_c^{415} remain as the only two unknowns in these

two equations for cloud-contaminated situations (Min et al. 2004).

However, the derived τ_c^{415} overestimates the actual COD because radiation is scattered into the instrument's FOV during MFRSR measurements due to strong forward scattering on cloud particles. In order to correct measurements for that effect, Min et al. (2004) calculated a data set of *simulated* MFRSR intensities during cloudy conditions using a plane-parallel, one-dimensional radiative transfer model. This data set has been used to derive a correct COD from apparent, overestimated COD (resulting from Eqs. 16 and 17 using the above described approach). For details regarding the correction for forward scattering the reader is referred to Min et al. (2004). They validated the derived COD also by using a radiation transfer model. Min et al. (2004) used the retrieved optical depths for clouds and aerosols as an input to the radiation transfer model and compared calculated values for diffuse and global irradiances with measurements from the MFRSR. Differences between modeled and measured values are lower than 6% and, hence, uncertainty of the derived COD is approximately 6% (Min et al. 2004).

4 Data and Methods

In the previous chapters an overview of the application of the COD, the theoretical derivation and the scientific approach to calculate the COD has been given. In the following chapter the practice of the study at hand is explicated.

First of all, the terminology used in this thesis will be elucidated. Three terms are used within this study, namely: optical depth (OD), aerosol optical depth (AOD) and cloud optical depth (COD) and it is essential to differentiate between these three terms.

The sun photometer used here and the cloud-screening algorithm, developed by Smirnov et al. (2000) and adapted by Wuttke et al. (2012), are designed to derive AOD. This is accomplished by measuring the direct solar irradiance and inferring total optical depth of the atmosphere by using the approach described in section 2.2, Eq. 2. As illustrated by Eq. 4, the total optical depth is a summarization of the single optical depths of several atmospheric constituents. Therefore, by subtracting the optical depths of unwanted contributors like ozone or nitrogen dioxide, AOD can be derived. However, this is only possible if the direct beam solar irradiation is not influenced by the presence of clouds. To assure the absence of clouds in front of the sun (i.e., in the field of view of the sun photometer) the above mentioned cloud-screening algorithm is used (for details see Smirnov et al. 2000).

When using this measurement approach during cloudy conditions a contribution to the total optical depth caused by clouds obscuring the sun is evident. The resulting OD is therefore a combination of AOD and COD. In order to derive values for COD, the contribution by AOD must be subtracted from the measured OD (reflecting the sum of aerosol and cloud optical depths). To summarize,

- the measured and processed value is an optical depth of aerosols and clouds (OD),
- the cloud-screened measurements represent AOD (only measurements when the sun is not obstructed by clouds), and
- during situations with clouds in front of the sun, the COD is calculated by subtracting a mean value for the AOD from the OD measurements. The mean value of the AOD is not constant and can be calculated, for instance, as a mean over the whole day on which the specific OD measurement was gathered:

$$\mathrm{COD} \;=\; \mathrm{OD} - \mathrm{mean}(\mathrm{AOD}).$$

In order to derive AOD information, Wuttke et al. (2012) employed the cloud screening algorithm from Smirnov et al. (2000) and only used measurements when the FOV of

the sun photometer was not influenced by clouds. It is conceivable that due to this cloud-screening the majority of OD measurements was rejected to calculate AOD. This dataset of cloud-contaminated AOD measurements has not been used for any scientific purpose so far. In order to bring this dataset to use, COD values will be calculated using the approach outlined above and illustrated in detail in chapter 4.2.1.

4.1 Instrumentation

As already mentioned in chapter 1.1 the data set used in this thesis was analyzed from Wuttke et al. (2012) in the first place. They characterized the AOD situation in Innsbruck. However, no studies investigating COD in the Alpine region are known to the author.

4.1.1 Measuring site

Optical depth is derived by ground based sun photometry in Innsbruck, Austria (47.2 6N, 11.3 9E, 620 m above sea level (asl)) since January 2007. The sun photometer and an all-sky camera (see chapters 4.1.2 and 4.1.3) are mounted on the roof of the Leopold-Franzens-University Innsbruck, a ten story building in the city center.

The measuring site is influenced by an urban boundary layer with a low to moderate pollution level (Wuttke et al. 2012). Innsbruck is located within the Alps in the Inn valley which is orientated in West-East direction. Complex terrain reaches up to 2600 m asl in the vicinity of Innsbruck. The town is situated at the junction of Inn and Wipp valleys which heads towards the Brenner pass. The heavy goods traffic along this major transit route across the Alps accounts for a great part of the air pollution in this area (Beauchamp et al. 2004). However, pollution levels are greatly influenced by local weather regimes (Ingold et al. 2001; Grabner 2003) like Foehn winds or the formation of cold-air pools in the valley. During anticyclonic and calm, clear nighttime conditions nocturnal cooling can form persistent cold pools leading to comparably high boundary layer aerosol concentrations (Harnisch et al. 2009). The concentration of near-surface pollutants and aerosols in the Inn Valley can be either decreased or increased by the breakthrough of Foehn (e.g., Seibert et al. 2000; Harnisch et al. 2009; Gohm et al. 2009). Beside these short-term mountain specific aerosol situations, for cloud-free situations a yearly aerosol pattern typical for an urban midlatitude site is present with low AODs in winter and high AODs in summer (Wuttke et al. 2012). This intra-annual variation is mainly caused by the lower atmospheric humidity in winter and higher humidity in summer (Peterson et al. 1981; Holben et al. 2001).

Clouds at the measuring site develop in the base setting of a westerly flow. Furthermore, they are strongly influenced by the surrounding mountainous terrain. The mountain ranges north and south of Innsbruck influence atmospheric processes by a wide variety of orographic effects, such as the formation of diurnal wind circulations in complex terrain (valley and slope winds), as well as the formation of Foehn winds or

cold-air pools. For example, the formation of Foehn winds can reduce cloud cover over Innsbruck. In contrast, the formation of cold pools and the associated inversion in the valley can lead to the formation of low stratus clouds in the valley (for more detail, see Zardi and Whiteman 2013).

Further, the mountains around Innsbruck limit the horizon and, therefore, no direct solar radiation reaches the sun photometer for high SZAs. However, the measurements with very high SZAs are eliminated during data quality control (see chapter 4.2). Moreover, the formation of optically thick convective clouds over the mountain tops during daytime can further limit sun photometer measurements because of the low radiation income. This problem especially occurs during the warm period when snow cover is absent on the mountain tops and the shortwave radiation income is sufficient to form slope winds and trigger convection. Furthermore, the above mentioned low stratus clouds formed during cold pool events also reduce the radiation income severely. While the sun photometer can not detect enough radiation under these conditions, the sun tracker can not follow the sun's disk anymore. Therefore, most measurements with convective clouds obscuring the sun and nearly all of the measurements during low stratus events are not taken into account during the presented investigations.

4.1.2 Sun photometer

Spectral direct solar irradiance (Wm^{-2}) is measured with a one-minute temporal resolution by using a four-channel precision filter radiometer (PFR). The instrument uses four wavelength channels at 368, 412, 500 and 862 nm. The nominal bandwidth of the channels is 5 nm and the field of view (FOV) has a full opening angle of 2.5° . The instrument has a weatherproof housing and the aperture is protected by a synthetic quartz window. To reduce sensitivity to temperature changes and aging of the interference filters the detector head is temperature-stabilized. This is achieved by an active Peltier type thermostatic system which keeps the temperature at 20° C ± 1° C over a housing temperature range from -30° C to +35° C. The housing temperature is measured and recorded for quality control during post-processing. An automated shutter exposes the detectors only during actual measurements (1.5 s every minute) in order to minimize the dose dependent degradation.

The specific instrument in use was developed at the World Radiation Center (WRC) Davos and is part of the Global Atmosphere Watch (GAW) program by the World Meteorological Organization (WMO). The GAW network features twelve background stations with identical instruments (Holben et al. 2001). Aerosol observation and analysis are one of the main foci of GAW. Furthermore the program aims to enhance the coverage, effectiveness and application of long-term aerosol measurements. GAW also seeks for cooperative research with other measuring networks such as AERONET (WMO cited 2016). Beside these operational networks, sun photometers

are globally employed to derive spectral AOD, precipitable water and to calculate the Ångström exponent α (Holben et al. 2001).

The PFR is mounted on a two-Axis Tracker/Positioner by Kipp and Zonen configured to operate as an active solar tracker. The angular resolution of its belt drive is $0.036°$, the accuracy is $< 0.1°$ and the repeatability for movement in the same direction is $< 0.05°$. Since the solar disc covers an angle of approximately $0.5°$ the specifications of the sun tracker allow for optimal capturing of the sun's disk in the FOV of the PFR (Wehrli 2008; Wuttke et al. 2012).

The tracker is additionally equipped with a sun sensor which divides its FOV in quadrants. While tracking the solar disk, it compares the lightness of these quadrants. For example, if the solar disk is located in one of those quadrants this specific one will exhibit the highest lightness due to the direct solar radiation. The tracker orientates the instrument in a way that the difference between lightness of the quadrants is minimal. In the optimal case the solar disk is then located inmidst the four quadrants. This FOV positioning (active tracking) is automatically executed during measurements. However, during overcast conditions with optically thick clouds, like low-stratus in the valley, diffuse radiation is prevailing, i.e. the solar disk is not visible, and the lack of sufficient direct solar radiation causes the tracking procedure to fail. The tracker will then be out of position. Errors in tracking are stored with the corresponding irradiance measurement for later data quality control (see chapter 4.2) (Wehrli 2008).

Data used in this thesis cover the period from 2007 to 2014. Due to calibration, a software bug and instrument removal for measurement campaigns at other sites, data is not continuously available. Measurements are missing for a period of three months in summer 2007, one month in summer 2008, three months end of 2010 and three months in winter 2012. Shortly before the instrument was set up in Innsbruck, calibration of the PFR was done at WRC, Davos, with the refined Langley plot method to determine the top-of-atmosphere signal V_0 from Eq. (1).

During calibration, a linear regression between direct solar irradiance measurements and the optical airmass m is used to infer a hypothetical radiometer output at TOA ($m = 0$). The intercept of the linear regression denotes this hypothetical instrument output (Blumthaler et al. 1996; Wuttke et al. 2012). The main uncertainties of the AOD retrieval originate from the determination of V_0. Therefore, the correct determination is of great importance (Kreuter et al. 2013). For future uses, Kreuter et al. (2013) developed an elaborate method for improved Langley calibration. However, their calibration approach was not used for the presented work.

4.1.3 All-sky camera

In order to gather information about the cloud situation in Innsbruck all-sky images are recorded, collocated with the sun photometer. The pictures are taken by a Canon

Powershot A75 and A520 with a fish eye lens from 2009 to 2011 and a Canon EOS500 with fish eye lens from February 2011 onwards. The all-sky images make up a nearly continuous time series as only few single days are missing. Photos are taken by the camera every full hour. This time resolution might be sufficient to determine cloud types, although cloud situation can be changing rather rapidly. Therefore, in connection to the one-minute resolution of the sun photometer measurements a higher temporal resolution for the all-sky images would be desirable as cloud types obscuring the sun can change enormously within the hour of two subsequent images.

4.2 Methods

4.2.1 Calculation of cloud optical parameters

The approach for calculating the OD is adapted from Wuttke et al. (2012) and changed for the purpose of extracting COD information from the existing data set. The spectral irradiance measurements from the sun photometer are subjected to quality control, inverse cloud screening and calculation of COD for the four wavelengths 368, 412, 501 and 862 nm to retrieve the Ångström coefficient α and the curvature parameter γ. This procedure will be elaborated in the following.

At first, sun photometer measurements at night are eliminated by setting the minimum voltage threshold to 0.0001 V. The remaining data is converted into Wm^{-2}. Optical depth is then calculated from the irradiance data according to Eq. 3. As described in chapter 2.2, information about the aerosol relative optical airmass, $m_{rel,a}$, as well as information on the relative optical airmasses and optical depths for Rayleigh scattering, O_3 and NO_2 are necessary to infer optical depth. The optical airmass of aerosol is approximated and set to the same value as for water vapor (Kasten and Young 1989). However, the influence of water vapor itself is not taken into account because its influence on the spectral radiation for the used wavelengths is negligible. For the determination of Rayleigh optical airmass the approach of Kasten and Young (1989) was used. The Rayleigh optical depth is determined according to Bodhaine et al. (1999). Their approach requires additional information on the air pressure at the measurement site, which is gathered by a CS100 Barometric Pressure Sensor by Campbell Scientific, Inc., installed at the measurement site. To estimate the influence of O_3 absorption on the measurements the approach of Komhyr et al. (1989) is used for the O_3 airmass. The optical depth of O_3 is computed by $\tau_{O_3}(\lambda) = a_{O_3} * \Omega$, where a_{O_3} is the band-weighted ozone absorption coefficient and Ω the ozone column. It is obtained daily from the Ozone Monitoring Instrument, mounted on NASA's Earth Observations System (EOS) Aura mission spacecraft (NASA cited 2016b). Optical airmass of NO_2 is assumed to be equal to that of O_3 and the NO_2 optical depth is calculated from a climatological mean of the column-integrated number density of NO_2, which is 2×10^{15} molec. cm^{-2} (Valks et al. 2011).

By using the above mentioned approaches the optical influence of O_3, NO_2 and Rayleigh scattering on the total optical depth have been determined. Therefore, it is now possible to deduce the remaining optical depth using

$$\tau_{\lambda,z} = \frac{1}{m_{rel,a}}(ln(\frac{I_{\lambda,z}}{I_{\lambda,TOA}}) + \tau_{\lambda,z,R}\ m_{rel,R} + \tau_{\lambda,z,O_3}\ m_{rel,O_3} + \tau_{\lambda,z,NO_2}\ m_{rel,NO_2}). \quad (18)$$

with $\tau_{\lambda,z}$ being the remaining optical depth, as defined in the beginning of chapter 4. It includes extinction by molecules, aerosols and clouds in the available measurements. Using a cloud-screening algorithm on the data set leads to a separation of cloud-free measurements (used to determine AOD) and cloud-contaminated measurements. Wuttke et al. (2012) used the cloud-screening algorithm from Smirnov et al. (2000), slightly modified for the conditions and site in Innsbruck. The modified algorithm considers variation not only in OD but also in the Ångström exponent α, which is calculated by linear regression between the derived OD and the corresponding wavelengths. The aim of Wuttke et al. (2012) was to filter out measurements contaminated by clouds. However, within the herein presented study, particularly these cloud-contaminated measurements are subject to investigation. Therefore, Smirnov's cloud screening algorithm has been adopted to account for that, as described in the following. The first two criteria of Smirnov were adapted without changes. When they apply, data are eliminated. In contrast, the third and fourth criterion were inversed, i.e. if the conditions of these criteria apply, the measurements are kept. The four criteria of the **inversed cloud-screening algorithm** used in the study at hand are listed in the following:

i) Criterion for exclusion: Measurements with an optical airmass $\geq$ 6.

Optical airmasses exceeding six occur just around sunrise and sunset, i.e. at high SZAs. On the one hand, data are excluded due to the mode of operation of the sun photometer's tracker at that time of the day. The tracker needs to adjust to the position of the sun for some minutes after sunrise. The first measurements are, therefore, undirected and can not be used.

On the other hand, in order to derive cloud types (see chapter 4.2.2) and optical properties of different cloud types (see chapter5), it is necessary that only one cloud type is obscuring the sun. Therefore, high optical airmasses, i.e., high SZAs, increase the chance of various cloud types obscuring the sun due to the longer path through atmosphere. These data were excluded from the presented analysis.

ii) Criterion for exclusion: OD $<$ 0.

Measurements that yield a negative OD are physically not meaningful but can arise from uncertainties in calibration and pressure and ozone measurements, which are used during the derivation of the optical depth. These data are, thus, not taken into account.

iii) Criterion for inclusion: Inverse triplet stability.

In their work, Smirnov et al. (2000) intended to eliminate *high-frequency* temporal instability of OD that may be traced back to cloud contamination. The data set with all four wavelengths is divided into sets of five timely consequent measurements spanning over five minutes, which are examined separately. The scenarios for a highly variable OD in the atmospheric column are:

- At least one of the five ODs exceeds a threshold value of 0.2 and at least two of the ODs vary by more than 0.03.
- No OD of the five exceeds 0.2 but at least two of the ODs vary by more than 0.03. Additionally, at least two of the corresponding Ångström exponents α vary by more than 0.02.

Measurements that fulfill these two requirements are assumed to be cloudy due to high fluctuations of the OD caused by the high variability of the cloud's optical properties. Thus, for AOD studies, measurements satisfying the two constraints are rejected. However, for COD studies all measurements that display high-frequency changes of OD are kept. Therefore, the herein presented work uses the inverse of this criterion of the cloud-screening algorithm by Smirnov et al. (2000).

iv) Criterion for inclusion: Inverse smoothness criterion.

The smoothness criterion of the cloud-screening by Smirnov et al. (2000) has been designed to remove *diurnal* variability of OD measurements. The procedure is as follows:

- If the standard deviation of all OD measurements from one day is below 0.015 all data are retained.
- Otherwise, if the standard deviation of the day's OD is above 0.015, the second derivative with time of the OD is examined.

  The second derivative describes the variability of the rate of change of the OD and is, therefore, very sensitive to local oscillations of optical depth caused by clouds. Smirnov et al. (2000) introduced a certain threshold value from empirical observations for the second derivative in order to decide whether or not cloud-induced diurnal variability of the OD occurs.

  - If the second derivative of the daily OD time series exceeds the threshold, which indicates cloud contamination, measurements are excluded from the dataset.
  - On the contrary, if the second derivative stays below the threshold, measurements are retained, even if the daily standard deviation is below 0.015.

For COD studies, however, the inverse procedure is applied: OD retrievals on days with a standard deviation *above 0.015 are retained*. If the OD standard deviation of that day is below 0.015 the second derivative is examined. In contrast to Smirnov et al. (2000), cloud-contaminated situations are included, i.e. the second order derivative of the OD retrieval exceeds the threshold of the algorithm of Smirnov et al. (2000). For a more detailed description of the smoothness criterion the reader is referred to Smirnov et al. (2000)

Additionally to these four criteria, the sun photometer tracking error (see chapter 4.1.2) is inspected. If the sun tracker can not detect the sun's disk, for example, due to thick clouds or tracking geometry error, the sun photometer measurements are likely to be undirected and, therefore, not used.

After applying the above mentioned criteria of the cloud-screening algorithm and considering sun tracking errors the data set has been quality controlled and only contains cloud-contaminated measurements. Additionally, the extinction by Rayleigh scattering, ozone and nitrogen dioxide has been taken into account. However, the influence of aerosols on the total optical depth is still included in the OD calculations. Thus, for the computation of the COD a straightforward approach is employed. The COD is derived from a specific OD measurement by subtracting a *daily mean* of all AOD measurements on that specific day from the OD:

$$\mathrm{COD} \;=\; \mathrm{OD} - \mathrm{mean}(\mathrm{AOD}).$$

However, if AOD information from the specific day is missing (due to cloud contamination or tracking errors), a daily mean value of AOD measurements from the day before is used instead. If AOD measurements on the day before are also not available OD measurements of the specific day are discarded.

It is hypothesized that the daily mean AOD is a sufficiently good approximation for the AOD situation in the very moment of a single measurement, due to the different time scales of clouds and aerosols (Min et al. 2004; Guerrero-Rascado et al. 2011). Aerosol conditions vary on time scales on the order of days, while cloud situations change more abruptly, with time scales on the order of minutes to hours. An analysis of the AOD measurements revealed that the AOD is relatively constant over the course of most days but AOD also varies up to 0.2 during specific days. This variation limits the applicability of the proposed approach. However, as only single days show a more variable AOD only single measurements are affected and the overall impact of the imposed error seems rather small. In summary, the remainder after the subtraction is hypothesized to represent the COD. However, the subtracted daily mean AOD rather needs to be interpreted as an approximation for the aerosol influence and does not represent the actual influence of aerosols on the OD during a very measurement. This

is a potential error source for the COD value.

Especially for thin clouds with a low COD the influence of the AOD approximation during the COD calculation can produce large errors. Therefore, three **criteria for the resulting COD** are introduced:

i) Exclusion criterion: COD $<$ 0.1.

On one hand, physically not meaningful negative values can occur by the chosen approach to derive COD. For example, if optically thin cirrus (low COD) are assumed to be present in the morning in a very clear atmosphere (low AOD), this results in low OD values for these morning measurements. If it is assumed, that due to daily emissions the aerosol loading and, in turn, the AOD increase heavily over the course of the day, the daily mean AOD might exceed the specific low morning AOD values. This can result in negative (unphysical) COD values for the hypothesized morning situation characterized by optically thin cirrus clouds. On the other hand, taking the daily mean value of AOD measurements into account instead of the actual aerosol influence during the measurement introduces an uncertainty in the COD retrieval. Therefore, it is impossible to retrieve very low CODs with this approach and all derived COD values below 0.1 are ignored during the analysis.

ii) Exclusion criterion: COD $<$ 2 $\times$ mean(AOD).

Aerosol conditions in Innsbruck are characterized by daily mean AOD values reaching from 0.03 to 0.5 (Wuttke et al. 2012). Using the above described approach COD = OD $-$ mean(AOD), it is conceivable that the COD uncertainty, as well as the lowest inferable COD value are determined by the aerosol situation and its variability on a specific day. Therefore, in order to further reduce the number of error-prone COD values, all CODs that are smaller than twice the respective daily mean AOD are excluded from the data set.

iii) Exclusion criterion: Availability of at least five consecutive COD retrievals.

In order to further improve data quality, the retrieved COD values, with a one-minute temporal resolution, are averaged over five minute intervals. If less than five consequent COD retrievals are present averaging cannot be applied and these measurements are eliminated from the data set. This criterion is employed to eliminate highly temporally variable broken cloud situations.

In a next step the Ångström coefficients α and γ are determined. The Ångström exponent α is calculated by linear regression between the natural logarithm of the COD and the natural logarithm of the four wavelengths used by the PFR, 368, 412, 501 and 861 nm (see Eq. 7). The curvature parameter γ is derived by a non-linear

least squares fit of the naturally logarithmed COD and the natural logarithm of the four wavelengths, according to Eq. 8. However, it should be kept in mind that the basis of the above computations is formed by an approach for aerosols, Ångström's turbidity formula (Eq. 6), and is now applied to cloud particles. The most remarkable differences of scattering by cloud particles to scattering by aerosols is the enhanced forward scattering for water droplets, the Mie scattering on nonspherical particles like small ice crystals and the geometric scattering on large particles like ice crystals as mentioned in chapter 2.3.

4.2.2 Cloud type determination from photos

Fish eye photographs of the whole sky over Innsbruck for the years from 2011 to 2013 were visually analyzed to determine the cloud types obscuring the sun during PFR measurements. The cloud types Cirrus, Cirrostratus, Cirrocumulus, Altostratus, Altocumulus, Stratus, Cumulus, Stratocumulus are taken into account.

However, some constraints limit the cloud type determination:

- The sun's disk appears larger in the images as it is in reality due to overexposure. On the LCD chip of the camera also the neighboring pixels are stored as white and, hence, the image is not meaningful around the sun's disk. Therefore, only clouds covering a greater fraction of the sky including the solar disk are taken into account for classification.

- The aforementioned issue of low time resolution of the photographs (chapter 4.1.2) is addressed by considering only situations when the same cloud type is observed for more than two subsequent images (two hours).

- Further, if the sun is low above the horizon and clouds are present the probability for multiple cloud types within the sun-PFR-path increases. Therefore, it is impossible to assign the retrieved COD to a single cloud type. Hence, the photos in between one to two hours after sunrise and before sunset are not taken into account.

- Moreover, it is nearly impossible to identify the cloud base height from the photographs alone. Cirrus, Cumulus and low Stratus clouds can be determined rather explicitly but especially for differentiating between Stratocumulus and Altocumulus additional height information is needed. Therefore, cloud base height for Innsbruck from an online weather observations archive (Pogodi cited 2016) is used in combination with the fish-eye photographs for selected cases.

After the determination of cloud type events, the cloud types are assigned to the corresponding COD retrievals. This generates a new data set comprising CODs of different cloud types. However, it is important to keep two things in mind: Firstly,

this new data set contains only data from 2011 to 2013 whereas the original CODs for all cloudy moments ranged from 2007 to 2014. Secondly, the CODs assigned to the specific cloud types are no continuous time series anymore but a collection of COD time ranges with that specific cloud type obscuring the sun.

5 Results

5.1 Calculated COD values in Innsbruck

In the following chapter the results of the COD retrievals employing the above described approach are presented. The retrievals are based on data gathered with a PFR in Innsbruck with a one-minute temporal resolution for situations with clouds obscuring the sun during the period from 2007 to 2014. As shown in table 2, 70,349 COD values passed the cloud-screening and quality control. After applying the five-minute average and eliminating COD values that do not have at least four measurements consecutively before or after, 5,282 COD measurements remain for further investigation. The individual COD values are later assigned to several cloud types and this will be outlined later in chapter 5.2.

In order to gain an overview, Fig. 10 shows the optical properties of clouds in front of the sun for the period from 2007 to 2014. As mentioned in chapter 4, data gaps with a duration between one and three months are present in 2007, 2008, 2010 and 2012.

The top panel (Fig. 10a) depicts the calculated COD for measurements with clouds obscuring the sun at a wavelength of 501 nm. Many other studies concerned with AOD and COD derivations present their results for this wavelength. Therefore, this will also be shown throughout the presented thesis for the sake of comparability. However, most measurements at 368, 412 and 861 nm exhibit similar results and are therefore not shown. Retrieved COD values for the 501 nm wavelength show a mean value of 0.84 with a standard deviation of 0.45 and a median of 0.75 (see also table 3). The COD values range from a minimum of 0.1 to maximum values of 2.7. The minimum values of 0.1 are caused by the restrictive criterion which is employed in the derivation of the COD information and eliminates COD values below 0.1 (see chapter 4.2.1). In general, the measurements of the PFR detect only optically thin clouds with COD < 3, as defined by Guerrero-Rascado et al. (2011).

The derived COD values show a distinct seasonal variation (see Fig. 10a). The maximum values in the summer months are around two, whereas the maximum values in winter only reach approximately one. The reason for this at first surprising strong variability is twofold:

On the one hand, the annual cycle of the relative aerosol optical airmass $m_{rel,a} = 1/cos(\theta)$, with the solar zenith angle θ, leads to higher potential radiation income in summer than in winter (see Fig. 11). For example, the mean global solar irradiance in Innsbruck in June is 229 Wm^{-2}, whereas in December it is 45 Wm^{-2} (Peterlin 2006). Hence, for low SZAs in summer optically thicker clouds can be potentially translucent due to the higher radiation income. In contrast, clouds with the same

Table 2: Number of all COD measurements for the period from 2007 to 2014 and number of single COD measurements which have been assigned to different cloud types, but only for the period from 2011 to 2013. The number of cloud events has been determined by analyzing the all-sky images from 2011 to 2013. The number of cloud events refers to the total number of continuous time frames during which only a single cloud type was apparent in the all-sky images. The number of measurements left after applying the cloud-screening and quality control procedure (CSQC), or, as applicable, cloud-screening, quality control and the application of a five-minute mean (QSQC5MIN), are shown in the two rightmost columns. The different cloud types are further discussed in chapter 5.2.

	# cloud events	# CSQC	# CSQC5MIN
all cloud meas.	-	70349	5282
Ci	133	917	87
Cs	56	2040	264
Cc	7	172	13
St	3	2	0
As	17	301	32
Sc	87	2186	84
Cu	13	112	0
Ac	48	1437	68

optical characteristics in winter extinguish all radiation because of lower radiation income due to higher SZAs.

On the other hand, sensor sensitivity limits the amount of radiation that can be measured using the sun photometer (see chapter 4.1.2). Therefore, with optically thick clouds obscuring the sun at high SZAs, incoming radiation is below the sensor sensitivity. Thus, by using the present instrumentational setup no COD values exceeding one can be inferred in winter during conditions under which the optical airmass exceeds three.

This variation of radiation income is especially obvious for the annual cycle but is also present for the diurnal cycle. For example, the range of SZAs occurring in winter is also included in a summer diurnal cycle for a rising and setting sun. Therefore, also

Table 3: Statistical information for three parameters: Cloud optical depth (COD) at 501 nm, Ångström exponent α and curvature coefficient γ. The table lists minimum, mean and maximum values together with standard deviations (SD). Numerical values for both the 10^{th}- and 90^{th}-percentile and the median of the observational distribution are listed as well.

Parameter	Min.	Mean	Max.	SD	10^{th}-perc.	Median	90^{th}-perc.
COD (501 nm)	0.10	0.84	2.64	0.45	0.36	0.75	1.47
α	−0.82	−0.05	1.99	0.22	−0.23	−0.08	0.10
γ	−3.02	0.02	6.52	0.21	−0.06	0.02	0.09

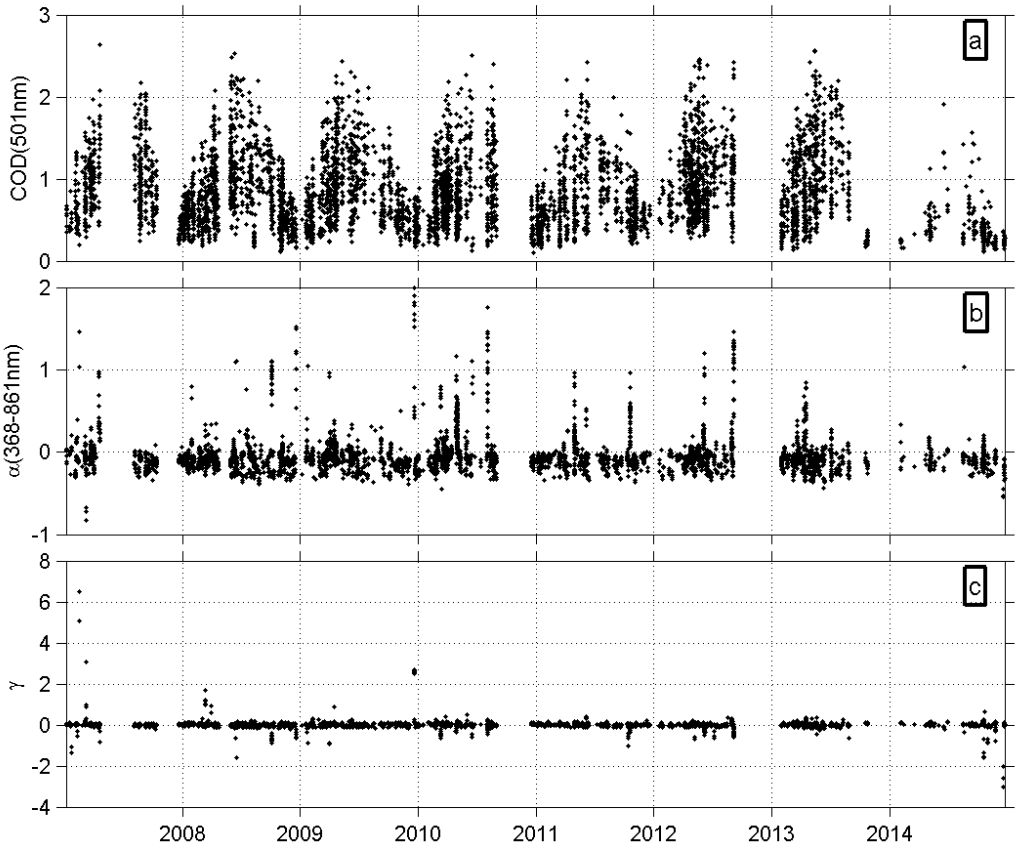

Figure 10: Cloud optical properties in Innsbruck from 2007 to 2014: a) Cloud optical depth at 501 nm, b) Ångström exponent α from the PFR wavelengths 368, 412, 501, 861 nm and c) the curvature coefficient γ.

for high SZAs in summer (i.e. morning and evening), the measurement of higher CODs is restricted by the sensor sensitivity when clouds obscure the sun. In general, with a more sensitive instrument also higher values of COD could be inferred for high SZAs, in summer and especially in winter. However, if the solar disk is not visible through the clouds the sun tracker can not track the solar disk and a tracking error is recorded.

O'Neill et al. (2000) proposed to present retrievals of AOD values with a lognormal probability distribution. They also use the geometric mean $\mu_g = \sqrt[n]{x_1 \cdot x_2 \cdot x_3 \cdot ... \cdot x_n}$ and geometric standard deviation $\sigma_g = \exp\sqrt{\sum_{i=1}^{n}(ln\frac{x_i}{\mu_g})^2/n}$ to describe the value distribution. A lognormal distribution can also be employed to characterize the retrieved COD values herein, as shown in Fig. 12 for the 501 nm wavelength (solid gray line). However, the range of derived COD values is limited by i) the minimum value criterion COD > 0.1 (see chapter 4.2.1) and ii) by the capabilities of the retrieval technique itself. The COD in winter is restricted to values below one and in summer the maximum possible retrievable COD is approximately 2.6. This is a synthetic annual variability caused by the limited sensitivity of the Sun photometer. It is assumed that these

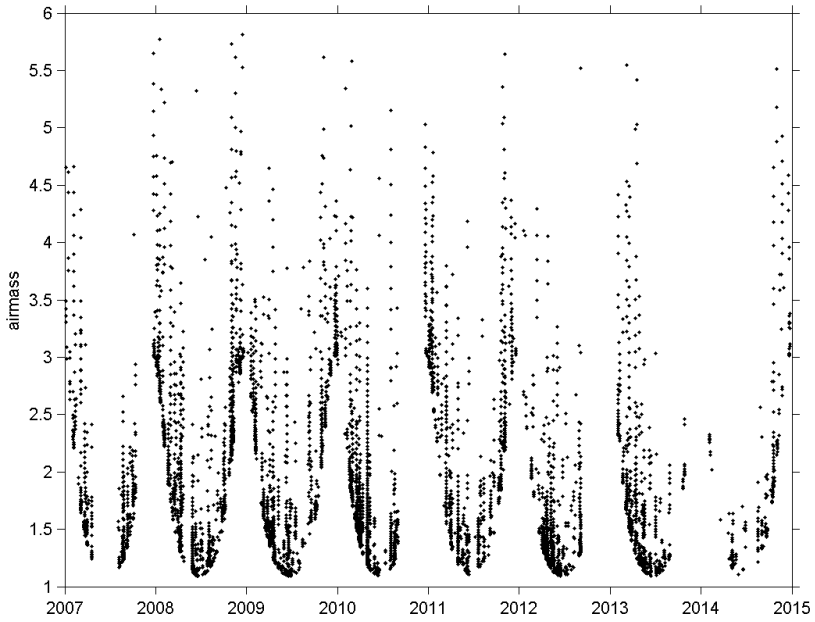

Figure 11: Optical airmass corresponding to the COD measurements depicted in Fig. 10 in Innsbruck from 2007 to 2014.

measurement restrictions also result in the positively skewed COD distributions shown in Fig. 12. Therefore, it is emphasized that the histogram of all retrieved COD values in Fig. 12a does not reflect the 'true' statistics of the COD for thin clouds. The histogram shows only the detectable CODs by the instrument and it is not possible to decide which values are connected with high or low airmasses. The CODs of two measurements are only comparable if they were retrieved during the same airmass situations. Thus, the COD statistics is additionally examined in three airmass categories, shown in Fig. 12b with airmasses $m < 2$, Fig. 12c with $2 \leq m < 3$ and Fig. 12d with $m \geq 3$.

The histograms in Fig. 12 clearly show that the proposed retrieval approach only works for optically thin clouds (COD below three). For Fig. 12d only CODs with corresponding airmasses above three were considered. Nearly all of these values were retrieved in the time from October to March but only few measurements are available. The COD ranges from 0.10 to a maximum of only 0.92 and displays a geometric mean of 0.41 (solid black line). For retrieving CODs above 0.92 the sensitivity of the instrument is too low for the given high airmasses. Figure 12c shows the frequency distribution of the COD for airmasses between two and three. The COD values exhibit a minimum of 0.11, a maximum of 1.38 and a geometric mean of 0.56. The values originate from measurements mainly from September to April. The most retrieved COD values correspond with airmasses below two, shown in Fig. 12b. These COD

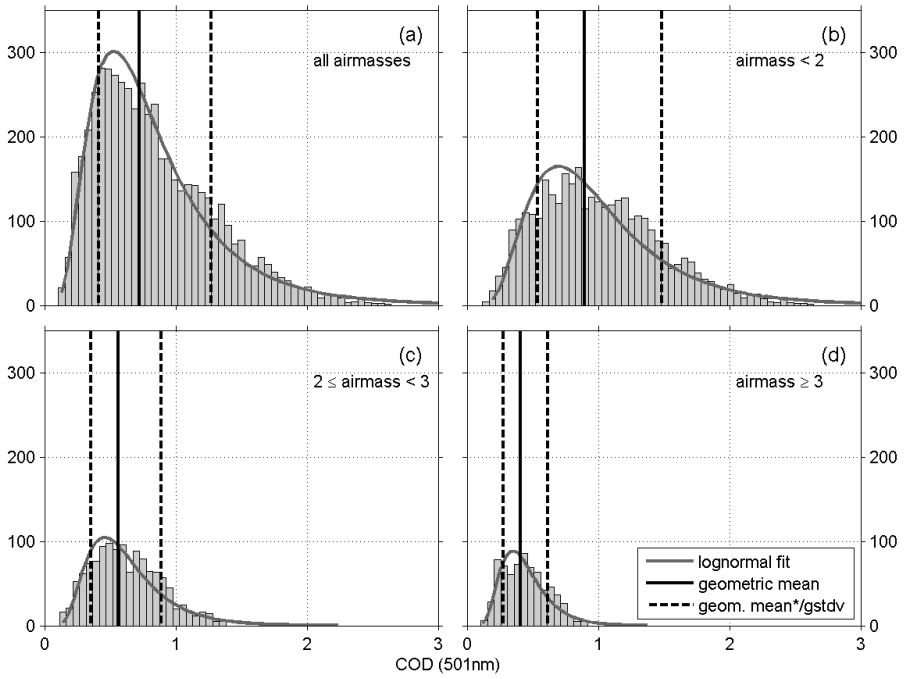

Figure 12: Histograms of COD for the wavelength channel 501 nm for different airmass ranges. (a) All data, a total number of 5282 measurements. The value distribution is characterized by a geometric mean of 0.72 (solid black line) and a spread due to the geometric standard deviation of 1.76 (dashed black lines at 0.41 and 1.27, respectively). The solid gray line represents a lognormal fit, that agrees well with the COD retrievals. (b) Airmass $m < 2$: the geometric mean is 0.90 and the geometric standard deviation 0.60 with a spread from 0.54 to 1.48. (c) Airmass $2 \leq m < 3$: the geometric mean is 0.56 and the geometric standard deviation 0.63 with a spread from 0.36 to 0.89. (d) Airmass $m \geq 3$: the geometric mean is 0.41 and the geometric standard deviation 0.67 with a spread from 0.27 to 0.61.

values are recorded between April and September. The COD distribution ranges from 0.12 to 2.64 and features a geometric mean of 0.90. The COD histogram of all retrieved values in Fig. 12a has a geometric mean of 0.72, a geometric standard deviation of 1.76 and a COD range from 0.10 to 2.64. The COD distribution of the 'summer values' between April and September (Fig. 12b) represents the distribution of all values in (Fig. 12a) in the COD value range very well (0.10 to 2.64 for all values, 0.12 to 2.64 for the 'summer values'). The geometric mean of the 'summer COD histogram' in Fig. 12b (0.90) is slightly higher than that of all CODs (0.72) due to the separation from the low COD values for higher airmasses (see Figs. 12c and d). However, despite this difference the 'summer COD histogram' is an acceptable representation of the COD statistics of thin clouds investigated herein.

The COD histograms derived using the four different wavelengths of the PFR behave very similarly (not shown). However, simultaneous measurements of the four different wavelengths do not necessarily result in the same COD. This spectral difference is analyzed in the following employing the Ångström exponent.

Figure 10b shows the Ångström exponent α corresponding to the cloud-contaminated PFR measurements. It is calculated from measurements using four wavelengths (368, 412, 501 and 861 nm) following the procedure illustrated in chapter 4.2.1. Maximum values of α are around two while the minimum values are negative, down to -0.8. The majority of the values range from -0.2 to 0.1 with only 10% of the values below -0.23 (10^{th}-percentile) and a 90^{th}-percentile of 0.1, as is shown in table 3.

Ångström's turbidity formula (see Eq. 6) states that the wavelength exponent α is determined by the spectrally varying AODs (or CODs herein). The Ångström exponent equals the numerical value of the negative slope of the linear relation between the logarithms of the wavelengths used for the PFR measurements and the logarithms of the corresponding retrieved AODs/CODs. A positive α results when the AOD/COD decreases with wavelength. This decrease is the stronger the smaller the particles are or the higher the fraction of small particles is, e.g., for Rayleigh scattering on air molecules ($\alpha = 4$). For larger particles, the spectral difference of the retrieved AOD/COD values diminishes, resulting in low values of α down to zero. This implies that the scattering regime changes from Rayleigh to Mie scattering (see chapter 2.3). When α equals zero the measurements have no wavelength dependence.

However, some aerosol studies have shown that experimental and statistical uncertainties can lead to AOD retrievals connected with a negative α (e.g., Arola and Koskela 2004; Estupinan 2006). Miller et al. (2003) note that a negative α for AOD retrievals might be connected with Mie scattering on liquid and ice particles in an otherwise relatively clear atmosphere (low AOD). In such a situation differential absorption by water or ice particles might occur with nearly no extinction in the short VIS (blue-green) and much stronger absorption in the NIR spectral region, resulting in a negative value for α.

As shown in Fig. 10b the Ångström exponent α retrieved in this study exhibits positive and zero values as well as negative values. All these values are related to single COD retrievals (with individual cloud situations). The spectral behaviour of three different COD retrievals and the corresponding α is exemplary shown in Fig. 13. On the one hand, if the derived COD *decreases* with wavelength (retrieved COD is higher for 368 nm than for 861 nm, red line in Fig. 13), α is *positive*, i.e. attenuation of radiation is stronger in the VIS than in the NIR spectrum. On the other hand, if the COD *increases* with wavelength α becomes *negative*, i.e. attenuation of radiation is weaker in the VIS than in the NIR spectral range (black line in Fig. 13).

The substantial amount of α values between -0.2 and 0.1 suggests (within aerosol theory) a high fraction of large particles. The typical radii of large aerosols are in the range from 0.2 to 2 μm. Cloud drops can reach sizes between 1 and 12.5 μm and ice crystals can be even larger, 1 to 1500 μm (see table 1 and Lohmann et al. 2016). Therefore, cloud particles can exceed the size of aerosols by far. As this study examines

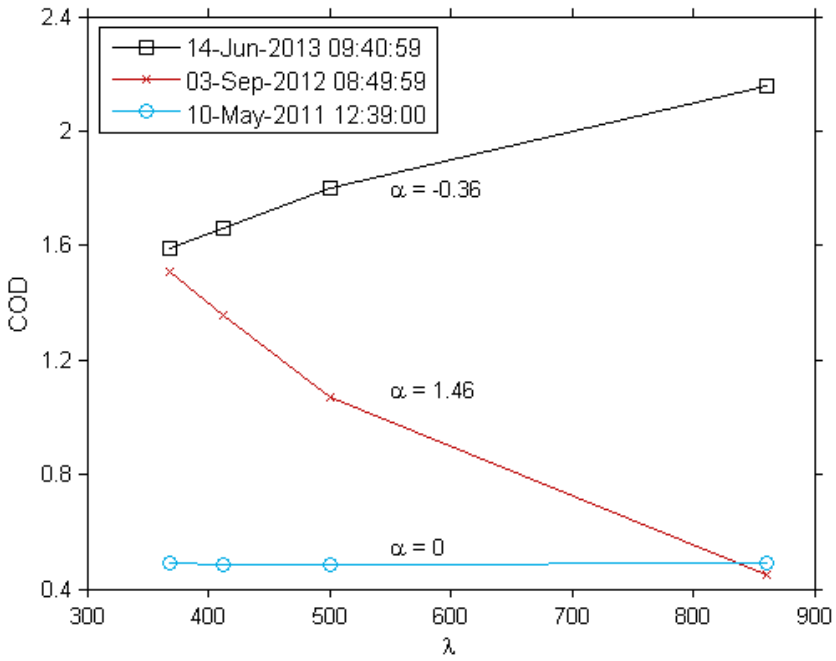

Figure 13: Examples for the dependence of the COD on the wavelengths used for the measurement. The corresponding Ångström exponent α is also denoted. The shown measurements are taken from the cloud-contaminated dataset illustrated in Fig. 10.

cloud-contaminated PFR measurements, hydrometeors are naturally present and Mie scattering occurs.

Figure 7 and 8 in chapter 2.3 show that extinction efficiency (Q_{ext}) exhibits a wave-like structure depending on the size parameter. Overall, the variability of Mie extinction efficiency decreases with size parameter (Fig. 7b) and approaches a value of two for increasing size parameter. However, the range between $\chi = 1$ and, for example, $\chi = 40$ shows high variability. In turn, the scattering efficiency of a given single particle can either increase, decrease or even stay approximately the same, depending on the exact wavelengths and, hence, size parameters during measuring.

On the one hand, if the size parameters of one (multi-channel) measurement, resulting from a given particle size and the different measurement wavelengths, are within a narrow range like from 6 to 11, extinction efficiency decreases with size parameter (blueing on a single falling slope, see Fig. 7a). On the other hand, if the size parameters cover a wider range (for instance, 15 to 60) an *overall* decreasing extinction efficiency can be found. This situation is schematically illustrated in Fig. 7b. However, the high variety of size parameters during cloud-contaminated PFR measurements (see table 4) shows that a wide variety of Mie scattering efficiencies can occur. It is conceivable that under certain conditions (like χ_5 to χ_8 in Fig. 7b) an *increasing extinction efficiency* for a *decreasing size parameter* (and, therefore, an *increasing* extinction efficiency for an *increasing wavelength for a given particle size*) can occur. This would imply a *negative*

Table 4: Size parameters $\chi = \frac{2\pi r}{\lambda}$ for cloud particle radii (r) of Cirrus/Cirrostratus and Stratocumulus/Altocumulus and the respective maximum and minimum wavelengths used in this study of 861 nm and 368 nm.

Cloud type	r (μm)	Size parameter $\chi = \frac{2\pi r}{\lambda}$	
		$\lambda = 861$ nm	$\lambda = 368$ nm
Ci, Cs	1	7	17
	100	730	1707
	1500	10946	25610
Sc, Ac	2	14	34
	4	29	68
	10	73	171

value for α. It is hypothesized that the interplay between the wavelengths used for measurements and different particle sizes (i.e., the high variability of the size parameters) can cause a multitude of several combinations of Mie extinction efficiencies. This, in turn results in slightly different spectral CODs and, hence, values for α. Therefore, the wave-like structure of Mie extinction efficiency is hypothesized to be responsible for negative Ångström exponents in Fig. 10b. However, for even larger spherical particles the spectral variability of the extinction efficiency decreases ($Q_{ext} \approx 2$ for high size parameters in Fig. 7), yielding $\alpha \approx 0$. Additionally, due to a high variability of particle sizes and, hence, size parameters within a cloud (see table 4) the exact extinction efficiency for a given measurement wavelength is more or less randomly distributed within the range given by Mie theory (Q_{ext} in Fig. 7).

The calculated Ångström exponent α, shown in Fig. 10b and 14, exhibits a variability between -0.3 and approximately 1.5 (see also table 3), which reflects the variation of atmospheric conditions during measurements. It is conceivable that in the small FOV of the PFR with opening angle 2.5° the cloud conditions can change rapidly. For example, cloud characteristics can change during measurements, including cloud type and thickness, and various cloud types one upon the other can occur. Furthermore, the size distributions of cloud particles can strongly vary within one cloud (Kokhanovsky 2004). The large positive values of α (up to two) connect to situations with small particles, whereas low α values result from larger cloud particles present in the atmosphere, as mentioned above.

However, Gobbi et al. (2007) point out that, with respect to *aerosol theory*, α alone does not provide unambiguous information on the relative weight of coarse and fine modes when determining the AOD. Large fine mode particles can have the same α as mixtures of coarse mode and small fine mode particles (Gobbi et al. 2007). Therefore, the curvature parameter γ is needed to provide additional information on the size distribution. In the following it is examined whether γ delivers valuable information

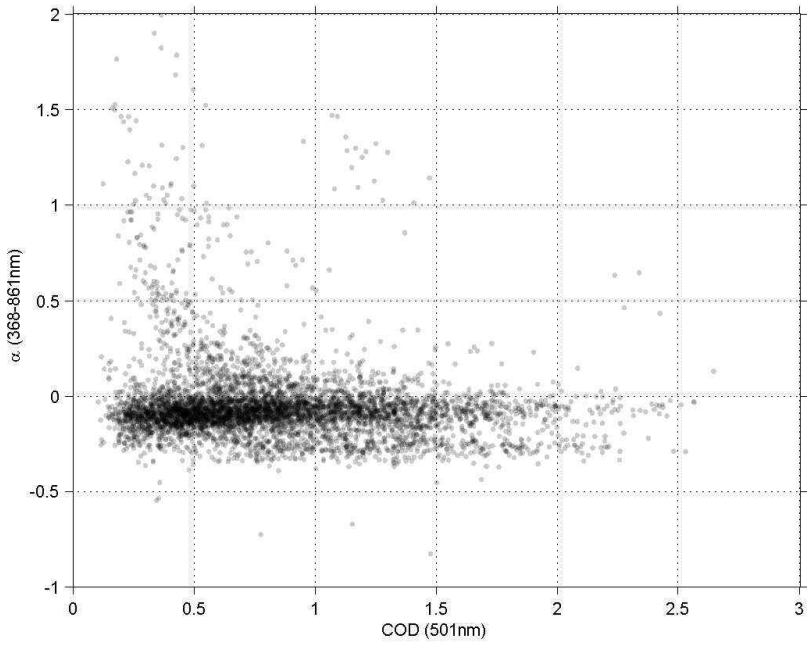

Figure 14: Cloud optical depth (COD) for the 501 nm wavelength channel in relation to the derived Ångström exponent α (calculated using the COD inferred from all wavelength channels, 386−861 nm) for each measurement (5282 in total).

on the size distribution of the cloud hydrometeors in the study at hand.

In Fig. 10c derived values of the curvature parameter γ are depicted. As described in chapter 2.2, the parameter γ accounts for the curvature in the wavelength-COD-relation. For aerosols, negative γ values account for aerosol distributions dominated by fine mode aerosol, i.e. particles of size $\lesssim 0.5\ \mu m$ like urban aerosol, whereas positive values indicate a significant fraction of coarse mode particles, i.e. particles $\gtrsim 0.5\ \mu m$ like mineral dust. The calculated values for γ in Fig. 10c are located nearly exclusively around zero with only some outliers in the positive (maximum of 6.5) and negative (minimum of -3). These extreme values have been examined separately to investigate the reason for these higher absolute values: The corresponding PFR measurements were conducted on different days and nearly all were gathered during time periods which exhibit a high portion of defective data (hence, measurements eliminated during quality control). Therefore, it is assumed that these extreme values are also erroneous and they are not considered any further.

The mean value of γ is nearly zero (0.02) and the 10^{th}- and 90^{th}-percentiles are -0.06 and 0.09, respectively. Details can be found in table 3. In general, the curvature parameter γ is ≈ 0 for nearly all measurements and, therefore, the wavelength-COD relation in the study at hand does not exhibit curvature. Hence, γ is not further taken into account during the following analysis.

The relation between the Ångström exponent α and the COD for the wavelength

501 nm, also investigated by Holben et al. (2001) and Wuttke et al. (2012), is illustrated in Fig. 14. Positive Ångström exponents occur mainly for a COD below 1. This finding agrees well with the assumption that the measurements with higher α could result from short moments exhibiting cloud-free conditions in front of the sun (i.e., measurements when the cloud-screening algorithm failed due to a highly variable cloud situation). This can happen, for example, in the very moment when one cloud is advected out of the area of the solar disc and the next cloud has not yet reached the area of the solar disc or moments when the sun was only partly obscured by clouds. Due to the fast alternation of radiation income at the sun photometer these data were not rejected by the inverse cloud-screening. However, the attenuation of radiation is mainly caused by aerosols in these cases and the corresponding values derived herein agree well with the AOD and α for aerosols described by Wuttke et al. (2012). Their Ångström exponents for aerosol in Innsbruck range from 0.5 to 2 for AODs from zero to 0.5 for *daily mean* aerosol situations. Therefore, for the purpose of describing cloud optical properties the focus of the study at hand is rather on the zero to negative Ångström exponents.

In contrast to the positive values of α which cover a wide range of numerical values (0 to 2 for a COD below 1), the COD-α-relation shows a distinct delimitation for negative values of α at about -0.3. This lower boundary is present for all CODs from 0.1 to 2.6 and there are nearly no measurements with an α beyond -0.3. The spectral extinction behavior of the investigated clouds seems to be barely dependent on the absolute value of the COD. This behavior is further discussed in chapter 5.2 and shown in more detail in Fig. 17.

Moreover, it seems that there are two modes of the Ångström exponent α. The first mode exhibits α values close to zero but yet negative (-0.1) and the second mode consists of slightly lower α values of about -0.3. It is hypothesized that ice and water clouds might be responsible for this difference. This is discussed further in the following chapter 5.2.

5.2 COD properties of different cloud types

The data set discussed in the previous chapter was gathered during conditions with clouds obscuring the sun. No distinction between different cloud types has been made so far. This chapter now aims to relate different cloud types to COD ranges and values of α. The procedure to determine different cloud types through all-sky images has been outlined in detail in chapter 4.2.2. Cloud type information is available for the period from 2011 to 2013. Numerous cloud events were recorded during these three years (see table 2). Within this thesis, a cloud event is defined as a continuous period of time during which only a single cloud type (for example, Cirrus) obscures the sun.

The most frequently detected cloud types are Cirrus (133 cloud events), Cirrostratus (56 cloud events), Stratocumulus (87 cloud events) and Altocumulus (48 cloud

events). The first reason for this is that these clouds often occur for a period longer than two hours due to their synoptic scale origin. Exceeding this time limit of two hours was a prerequisite for the clouds to be considered during the cloud type determination procedure. Secondly, these cloud types were translucent (i.e., optically thin) enough to allow for the passage of direct solar radiation and enable the sun photometer to detect incoming radiation. Thirdly, there are many time periods in which these cloud types occur singularly without other cloud types in front of the sun. This is also caused by their rather synoptic-scale origin. Cirrocumulus clouds (7 cloud events) did not persist long enough for detection in most cases, whereas Stratus (3 cloud events) and Altostratus clouds (17 cloud events) often were too optically thick to allow for the passage of enough direct solar radiation. In Innsbruck, Cumulus clouds (13 cloud events) occur mostly above the slopes of the surrounding mountainous terrain but were not observed very often in front of the sun.

After the cloud screening, calculation of the COD and quality control 917 (Ci), 2040 (Cs), 172 (Cc), 2 (St), 301 (As), 2186 (Sc), 112 (Cu) and 1437 (Ac) single COD measurements have been assigned to the respective cloud types (see table 2). The averaging over five *directly consecutive* measurements reduces the number of measurements to 87 (Ci), 264 (Cs), 13 (Cc), 0 (St), 32 (As), 84 (Sc), 0 (Cu) and 68 (Ac). The drastic decrease after averaging for nearly all cloud types is caused by the highly intermittent COD information which has been derived using the PFR measurements. For further investigation a threshold of at least 60 values of single COD measurements has been applied. Hence, in the following only the COD properties of Ci, Cs, Sc and Ac are investigated.

Figure 15 shows histograms of the COD in the 501 nm wavelength channel for the four cloud types Ci, Cs, Sc and As, normalized by the number of respective measurements for each cloud type. As mentioned for the histograms in Fig. 12 the COD measurements are taken during different airmass situations throughout the year. A separate examination of the different cloud type COD histograms divided into the three airmass categories mentioned above ($m < 2$, $2 \leq m < 3$, $m \geq 3$) showed, that measurements of Ci clouds are available for the three airmass classes in approximately the same frequency but very few (less than 30). In the two higher airmass classes ($2 \leq m < 3$, $m \geq 3$), not enough COD values of each cloud type are available for a statistical investigation (below 35 values). Cirrostratus, Stratocumulus and Altocumulus clouds feature the most COD values for the low airmasses ($m < 2$). Therefore, only the statistics of the COD distribution in the lowest airmass class is mentioned additionally to the COD statistics of all airmasses (in brackets behind the values with all classes included). Cirrus clouds exhibit exclusively COD values in the range of 0.2 to 0.7, see Fig. 15a (0.2 to 0.7 for $m < 2$). The geometric mean is 0.35 (0.4) and the values within one geometric standard deviation range from 0.25 to 0.5 (0.3 to 0.8). Cirrostratus

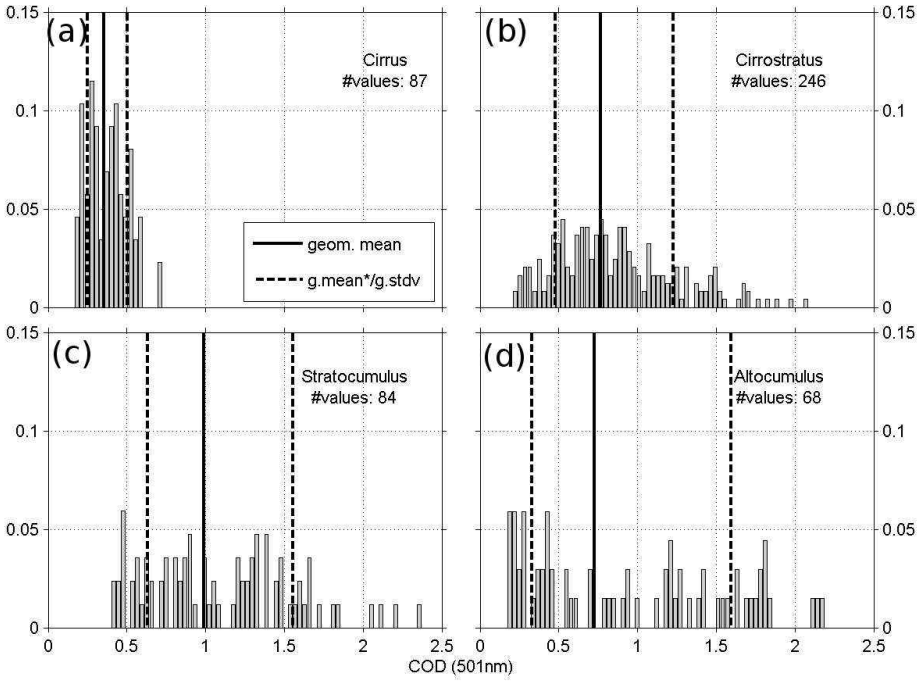

Figure 15: Histogram for the cloud optical depth (COD) of the 501 nm wavelength channel separated for single cloud types for the period from 2007 to 2014: (a) Cirrus, (b) Cirrostratus, (c) Stratocumulus and (d) Altocumulus. Each histogram is normalized by the number of respective measurements (noted on each panel). The solid black line indicates the geometric mean of the value range. Dashed black lines denote the numerical value of the gemetric mean plus, resp. minus one geometric standard deviation.

clouds exhibit a broader COD range from 0.2 to 2.2 (0.2 to 2.1), see Fig. 15b, reflecting that Cs can be geometrically and optically much thicker than Ci. The geometric mean is 0.8 (0.9). The Cs COD frequency distribution does follow a lognormal fit, as used in the histogram showing the COD values of all cloud-contaminated measurements (Fig. 12). The COD histograms of the other clouds types do not follow a specific distribution (see Figs. 15a, c and d). Stratocumulus CODs range from 0.4 to 2.4 (0.6 to 2.4) with a geometric mean of 1.0 (1.2). Altocumulus CODs range from 0.2 to 2.2 (0.7 to 2.2) with a geometric mean of 0.7 (1.4). The minimum value within the COD range of Sc clouds (0.4–2.4) suggests that these clouds are geometrically and, hence, optically thicker clouds compared to Ac (0.2–2.2) (Lohmann et al. 2016). All types, except Ci clouds do feature a broad COD frequency distribution. This is illustrated by the dashed lines in Fig. 15 which denote the value range within one geometric standard deviation from the geometric mean.

The corresponding histograms of α values are depicted in Fig. 16, also normalized by the number of respective measurements. As for Fig. 15 the statistics of the COD distribution in the lowest airmass class $m < 2$ is mentioned additionally to the COD statistics of all airmasses (in brackets behind the values with all classes included). The

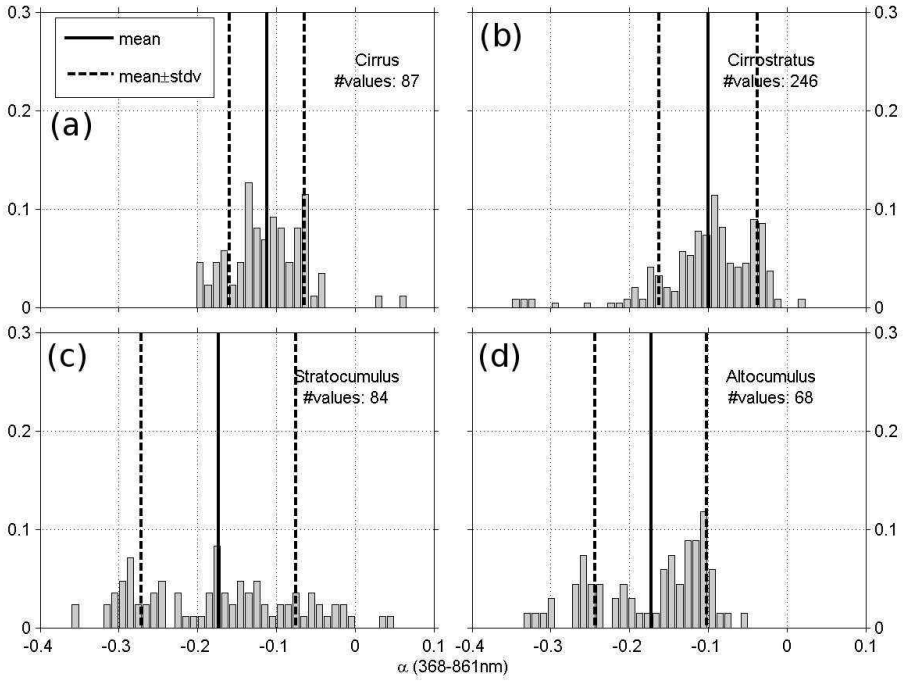

Figure 16: As Fig. 15 but for the Ångström parameter α.

Ångström parameter α is ≤ 0 for all cloud types for almost all measurements. The geometric mean value for ice clouds (Ci and Cs) in Figs. 16a and b is ≈ -0.1 (≈ -0.1), while Cs clouds do show a higher COD value range compared to Ci (see dashed lines in Figs. 16). A broader α frequency distribution is evident for the water clouds (Sc and Ac) in Figs. 16c and d. The Ångström parameter of Sc is nearly equipartitioned in the range from -0.35 to 0.04 (-0.35 to 0.04), which is broad compared to Ac clouds. The geometric mean for Sc clouds is -0.18 (-0.19). The herein presented Ac clouds (see Fig. 16d) feature α values from -0.33 to -0.05 (-0.32 to -0.08) and have a more pronounced peak of α values at about -0.1, compared to Sc clouds (see Fig. 16c). This cumulation of slightly negative values can also be seen in the histograms of Ci and Cs. A possible reason for this aspect is that Altocumuli can appear as mixed-phase clouds with liquid cloud drops as well as ice crystals (Lohmann et al. 2016).

Figure 17 combines information for the COD and α. The COD-α-distribution for Cirrus clouds (see Fig. 17a) clusters in 0.1 to 0.6 for COD and -0.05 and -0.2 for α. The optically thin Cirrus clouds are all connected to a slightly negative α and, therefore, to slightly higher extinction of radiation with longer wavelength (see chapter 5.1). However, the other three depicted COD-α-relations for Cs, Sc and Ac (see Fig. 17b, c and d) show a much different situation with the both parameters COD and α varying over a larger range.

The red line in Fig. 17 illustrates the linear correlation between the COD and α. The correlation coefficient is approximately zero for ice clouds (-0.05 for Ci and

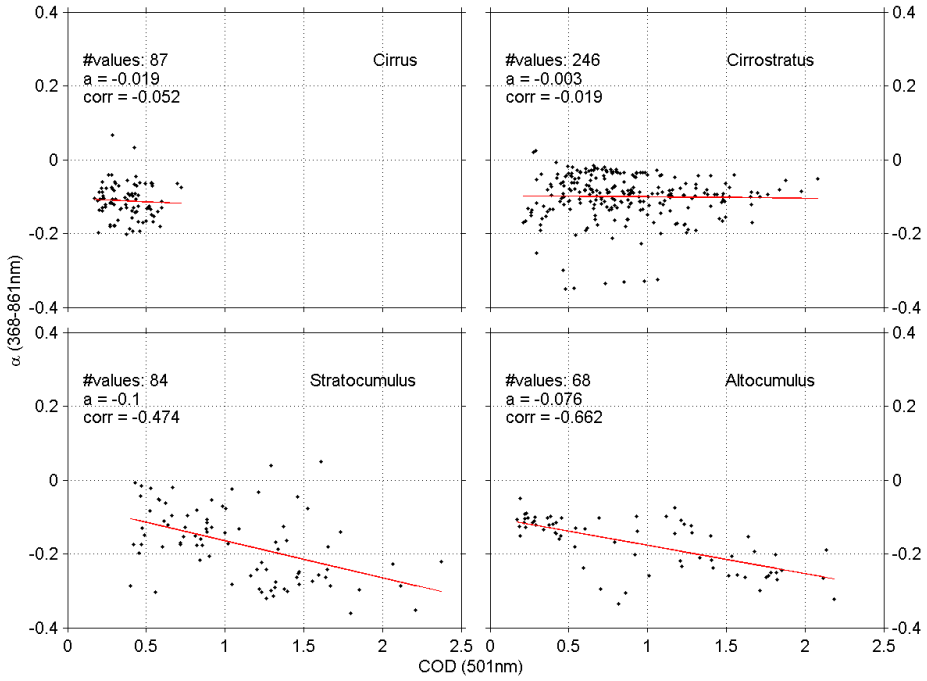

Figure 17: As Fig. 14 but separated for different cloud types: Cirrus (top left), Cirrostratus (top right), Stratocumulus (lower left) and Altocumulus (lower right). The number of measurements is noted on every panel, as well as the correlation coefficient (*corr*) and the slope (a) for a linear correlation of the measurements (red line in each panel).

-0.02 for Cs due to a large value spread). For water clouds (Sc and Ac) the correlation coefficient is -0.47 for Sc and -0.66 for Ac. The not existing correlation for Cs clouds is hypothesized to be also caused by the limited number of measurements and limitation of the instrumentation (sensitivity of the PFR). Nevertheless, the regression line shown in Fig. 17 is employed to indicate a possible trend that ice (water) clouds exhibit no (a negative) slope of the linear correlation. These trends also hint at the presence of the two modes relating to the COD-α-distribution in Fig. 14, as mentioned in chapter 5.1 .

The regression of the Ci clouds is not discussed further due to the clustering and the low linear regression coefficient. The slope of the regression line a is nearly zero for Cs in Fig. 17b with an intercept of $\alpha \approx -0.1$. Hence, the upper mode in Fig. 14 might be caused by Cs. Chapter 5.1 mentions that the lower mode of all cloud-contaminated measurements is constant at an α value of about -0.3. Figure 17c and d show that the COD-α-relations of Sc and Ac have slopes of approximately -0.1. Values of $\alpha \approx -0.3$ are mainly present for CODs above one. The COD-α-relations of Sc and Ac do, therefore, not completely explain the second mode but might influence the distribution in Fig. 14.

Chapter 5.1 explained that a negative α occurs due to an increasing extinction efficiency with increasing wavelength. It was stated that the exact extinction efficiencies

for the given measurement wavelengths are dependent on the size parameters and exhibit high variability within the range given by the Mie theory (see Fig. 7).

Typical sizes of cloud drop radii of water clouds like Sc and Ac range from 2 to about 10 μm (see table 1). Figure 8 shows the extinction efficiency of various spherical particles with a scattering behaviour similar to water. For drops with a radius of 1 μm the extinction efficiency varies between approximately 2.6 and 1.9 for the lower three wavelengths used in this thesis (368, 412 and 501 nm) but Q_{ext} is remarkably higher ($\approx$ 3.7) for the highest wavelength used (861 nm). This yields a negative α for the specific measurement. In Fig. 8, particles with radii of 10 μm exhibit less variability of the extinction efficiency but still slightly higher possible Q_{ext} values for higher wavelengths (and nearly no lower values because the minima of the wave-like distribution are almost constant at approximately two). In summary, the α values of 1 μm particles will be negative for the wavelengths used for measuring, whereas for particles with 10μm radii slightly negative or zero values for α are most likely.

The particle size range between 1 and 10 μm (including the typical radius of Ac and Sc cloud particles of 4 μm, see table 1) also exhibits mainly negative to zero values for α. For example, the size parameters for a 4 μm hydrometeor using wavelengths of 368, 412, 501 and 861 nm are, respectively, 68, 61, 50 and 29 (see table 4). These size parameters result in extinction efficiencies of about 2, 2.1, 2.1 and 2.3 (see Fig. 7). This small increase of extinction efficiency with wavelength yields a slightly negative Ångström parameter α for 4 μm sized water cloud drops.

Nonspherical particles, however, like most ice crystals can display a different extinction behavior than the one shown in Fig. 7 for spherical particles. Yang et al. (2013) derived scattering properties of various ice crystal morphologies and sizes in the spectral range from 0.2 to 200 μm. Figure 18 shows the extinction efficiency of nine different ice crystal habits with a size of 15 μm (Figs. 18a, b, and c) and 200 μm (Figs. 18d, e and f).

Figures 18a and d show the extinction behavior of columns and plates that mainly built up Cirrostratus and the top part of Cirrus clouds (Kokhanovsky 2004; Lohmann et al. 2016). The cloud base of Cirrus clouds consists mainly of spatial crystals like bullet rosettes and aggregates of ice crystals (Parungo 1995; Liou 2002). The scattering efficiency of those crystals is depicted in Figs. 18b, c, e and f. The figures show that the extinction efficiency of ice particles with a size of 200 μm is nearly constant for the wavelengths used for the presented measurements (368, 412, 501 and 861 nm). This implies that the Ångström exponent α is near or equal to zero for measurements influenced by such ice crystal shapes and sizes.

Smaller ice crystals with a size of 15 μm, as shown in Figs. 18a, b, and c, exhibit a higher variability of extinction efficiency with wavelength than the aforementioned larger particles. Especially the spatial ice crystals in Figs. 18b and c show a more

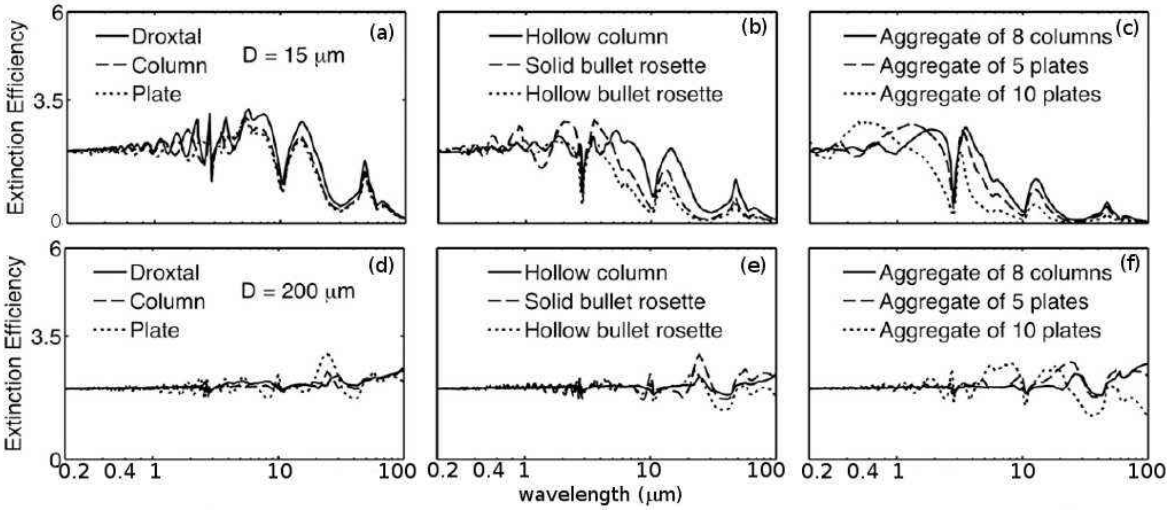

Figure 18: Wavelength dependence of the extinction efficiency for different ice crystal morphologies and sizes given for a wavelength range from 0.2 to 100 μm. Panels (a), (b) and (c) show the extinction efficiency for ice crystals with a particle size D=15 μm, while panel (d), (e) and (f) show the extinction efficiency for D=200 μm. Taken and adapted from Yang et al. (2013).

complex extinction behavior with extinction efficiencies ranging from 1.8 to about 3.0. For the spectral range used for measuring (360–860 nm) the increasing Q_{ext} indicates a negative α (see Figs. 18b and c). However, in ice clouds the number of crystals with a size of $> 200\mu$m is about two orders of magnitudes higher than the number of 15 μm-sized particles (see exemplarily Fig. 3). Therefore, the effect of the large particles might prevail resulting in zero and only slightly negative values for the Ångström parameter α.

If the extinction efficiencies for water and ice clouds are compared, small water droplets do show a higher maximum possible extinction efficiency ($Q_{ext,max} \approx 3.5$ for 1 μm drops) than small ice crystals ($Q_{ext,max} = 3$ for 15 μm crystals). Therefore, for water droplets possibly larger spectral differences of extinction efficiency result in stronger negative values for α. This emphasizes the above explanation for only slightly negative α for ice clouds and more negative α for water clouds in Fig. 14. This different behavior of ice and water clouds is hypothesized to be responsible for the linear trends in Fig. 17 and the two modes in Fig. 14. The upper mode is related to water and ice clouds but mainly to ice clouds, whereas the lower mode is connected to water clouds only (see also chapter 5.1).

In Fig. 14, a pronounced lower boundary for the Ångström parameter at -0.3 is shown for all inferred CODs. The α-COD-relation for different cloud types in Fig. 17 illustrates that the majority of $\alpha \approx -0.3$ is linked to the presence of Sc and Ac clouds. However, α of Sc and Ac is higher for small CODs and, therefore, the α-COD-relation for these cloud types do show a negative trend with increasing COD (see Fig. 17). Therefore, Ac and Sc clouds are only partly responsible for the distinct lower boundary in Fig. 14 for CODs exceeding one. It is possible that the pronounced lower boundary

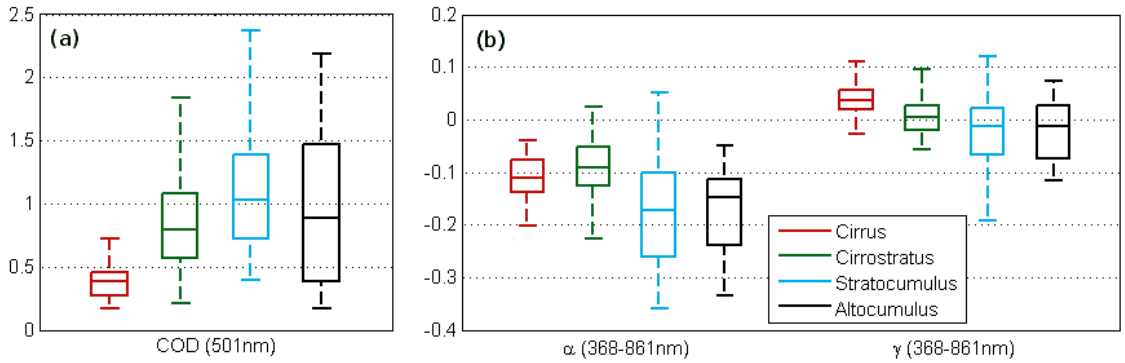

Figure 19: Boxplots of (a) the cloud optical depth (COD) for the 501 nm wavelength channel and (b) the Ångström parameter α and the curvature parameter γ for different cloud types: Ci (red), Cs (green), Sc (blue) and Ac (black). The central line in the boxes denotes the median, the edges of the boxes indicate the 25^{th}- and 75^{th}-percentiles and the whiskers extend to the most extreme data points.

of α in Fig. 14 is caused by multiple clouds that were not included in the manual all-sky image examination.

One reason for a decreasing α with increasing COD for water clouds could be multiple scattering. Within a cloud, the intensity of a (hypothetical) radiation beam decreases at every encounter with a cloud particle, scattering radiation out of the original (i.e., direct) sun-PFR-direction. If the extinction efficiency is higher for longer wavelengths (yielding a negative α), as it is the case for water clouds in the solar spectral range, every scattering event increases the relative difference between the CODs of short and long wavelengths. In geometrically thicker clouds multiple scattering is increased. Therefore, it can be assumed that α might decrease further for clouds with higher CODs. This might explain the negative correlation of COD and α in Fig. 14.

In contrast, the Ångström parameter for Cs clouds in Fig. 17b exhibits no wavelength dependency. It is conceivable that an ice cloud exhibits a wide variety of particle sizes (see Fig. 3). As mentioned above, ice particles with typical sizes for Cs clouds ($100-200$ μm, see table 1) exhibit a mainly wavelength-invariant extinction efficiency. On the other hand, smaller ice crystals do show a wavelength dependent extinction efficiency. With respect to multiple scattering, the interaction between radiation and larger particles does not influence the value of α, whereas, if smaller particles are involved in multiple scattering, α can become negative. However, as ice clouds consist mainly of larger particles, scattering on small particles has a minor influence on the value of α.

Figure 19 summarizes the optical parameters for different cloud types employing a boxplot. The central mark of the boxes indicates the median while box edges denote the 25^{th}- and 75^{th}-percentiles. Figure 19a shows the derived COD for the 501 nm wavelength channel for Ci (red), Cs (green), Sc (blue) and Ac clouds (black). Stratocu-

Table 5: Minimum, median and maximum values, as well as numerical verlues for the 25$^{\text{th}}$- and 75$^{\text{th}}$-percentile for cloud optical depth (COD, top panel), Ångström exponent (α, middle panel) and curvature parameter (γ, bottom panel) for different cloud types.

Cloud type	COD				
	Min.	25$^{\text{th}}$-perc.	Median	75$^{\text{th}}$-perc.	Max.
Ci	0.17	0.28	0.38	0.46	0.72
Cs	0.21	0.57	0.79	1.08	1.84
Sc	0.40	0.72	1.03	1.40	2.37
Ac	0.17	0.38	0.89	1.47	2.19

Cloud type	α				
	Min.	25$^{\text{th}}$-perc.	Median	75$^{\text{th}}$-perc.	Max.
Ci	−0.20	−0.14	−0.11	−0.08	−0.04
Cs	−0.22	−0.13	−0.09	−0.05	0.02
Sc	−0.36	−0.26	−0.17	−0.10	0.05
Ac	−0.33	−0.24	−0.15	−0.11	−0.05

Cloud type	γ				
	Min	25$^{\text{th}}$-perc.	Median	75$^{\text{th}}$-perc.	Max
Ci	−0.03	0.02	0.04	0.06	0.11
Cs	−0.06	−0.02	0.00	0.03	0.09
Sc	−0.19	−0.07	−0.01	0.02	0.12
Ac	−0.12	−0.07	−0.01	0.03	0.07

mulus and Altocumulus clouds feature COD values from 0.40 to 2.37 and 0.17 to 2.19, respectively (see table 5). However, Ac show a larger spread indicated by the 25$^{\text{th}}$- and 75$^{\text{th}}$-percentiles in Fig. 19a (see table 5). Cirrostratus clouds exhibit a COD range from 0.21 to 1.84 (see table 5). While the median value of the three aforementioned cloud types do show slight differences (see table 5) the total value ranges for CODs are comparable. In contrast, Ci exhibit lower COD values with a smaller range, from 0.17 to 0.72 with a median value of 0.38 (see table 5). In general, cloud types cannot be determined solely based on COD information due to the overlapping value ranges.

Figure 19b shows boxplots for the Ångström parameter α and the curvature parameter γ. Regarding α, Ci and Cs feature a similar value range from approximately -0.2 to approximately zero, while for Cs slightly positive values are possible (0.02), see table 5. Stratocumulus clouds also feature positive values for α (0.05) and show the largest value range, as Sc and Ac clouds exhibit lower minimal values for α (-0.36, resp., -0.33, see table 5). The lower α values of Sc and Ac compared to Ci and Cs are presumably linked to the different scattering behavior of water and ice clouds.

Figure 19b also shows the calculated curvature parameter γ. Cirrus clouds feature a positive value for the median (0.04), while other clouds types have a zero (Cs) or negative median (Sc and Ac, see table 5). Sc clouds exhibit the greatest value range (-0.19 to 0.07) which is also the case for the other parameters (COD and α). However, calculated values for γ are close to zero and, therefore, the curvature parameter can be neglected and is not taken further into account. Comparable to the situation for COD values in Fig. 19a, a distinct discrimination of clouds types, based on derived values for α and γ is not possible due to the overlapping value ranges.

6 Discussion and conclusions

Within the presented thesis a dataset of direct solar irradiance measurements, gathered in Innsbruck over the period from 2007 to 2014, was analyzed to derive optical parameters for clouds. However, the instrumentation was initially intended to derive aerosol optical depth (AOD) during *cloud-free conditions* but within this thesis an approach to retrieve cloud optical (COD) depth during *cloud-contaminated* measurements was developed. Numerous measurements with clouds obscuring the sun were gathered over the period from 2007 to 2014. After quality control and averaging over five minutes 5282 measurements were analyzed. Due to limitations of the measuring instrument, this was only possible for optically thin clouds, which are defined to exhibit a COD below three in this thesis.

It was shown that it is possible to derive COD information for cloud-contaminated PFR measurements. Inferred COD values in the 501 nm wavelength channel range from 0.1 to 2.64 and show prevailing values from 0.5 to 0.8. The upper delimitation of the COD is, as mentioned, caused by the sensitivity of the PFR, whereas the lower delimitation at 0.1 is due to a restriction criterion in the quality control. The COD frequency distribution is positively skewed and is well represented by a lognormal fit as suggested for the aerosol optical depth (AOD) by O'Neill et al. (2000). The cloud optical depth was retrieved using the following approach:

$$\mathrm{COD} = \mathrm{OD} - \mathrm{mean}(\mathrm{AOD}),$$

with OD denoting the optical depth retrieved by PFR measurements. During the OD retrievals, the extinction of NO_2, O_3 and Rayleigh scattering were taken into account while extinction by other atmospheric constituents was neglected, e.g. water vapor. Additionally, a plane-parallel and nonrefractive atmosphere was assumed during calculations. The overall effect of these simplification has not been determined but is assumed to be small. The resulting OD incorporates extinction by aerosols as well as clouds. Therefore, the effect of the AOD on the total OD was estimated using a straightforward approach employing a daily mean value of AOD measurements. AOD values are derived from measurements gathered by the same instrument during cloud-free conditions. It is conceivable that aerosol conditions change rather slow (timescale on the order of days), while the cloud situation shows high temporal variability (timescale on the order of minutes to hours). Therefore, it is possible to use a daily mean value for AOD to estimate the aerosol influence on single OD measurements. However, using the mean value introduces an uncertainty in the COD retrieval, as the AOD (501 nm) can vary by up to 0.2 on specific days. In order to address this problem in a future work, a time frame around a single cloud event could be defined involving AOD values

from before and after the event. Instead of taking into account all AODs of one day or the one before, the timely more relevant measurements can be used. This approach would allow for the detection of a possible change in the AOD during cloud events. Beside that, calculation of AOD daily mean values is on single days based on only few measurements. A small number of AOD measurements is generally present during days with mostly overcast sky and few moments with no clouds in front of the sun. Using a threshold of a minimum number of AOD retrievals for calculating the daily mean AOD would reduce the uncertainty caused by only few measurements.

This problem is illustrated in Fig. 20 which shows outlier values of the Ångström exponent α. The large values from 0.8 to 1.5 were derived for one day without cloud-free measurements (September 3 2012). The mean value for the AOD has been calculated using only five AOD retrievals from the day before (September 2 2012) which were rather low (AOD = 0.08 for the 501 nm wavelength channel and no significant spectral difference compared to other wavelength channels) while AOD measurements gathered on the September 4 2012 show a higher aerosol loading (AOD(501 nm) = 0.5) with a higher spectral difference between different wavelength channels (i.e., indicating also a change in the particle size distribution of the aerosols). Using only the low AOD retrievals from September 2 2012 leads to an underestimation of the AOD influence on the total optical depth and, hence, an overestimation of the COD. Additionally, the low spectral difference of the AOD retrievals on September 2 2012 lead to an overestimation of the spectral difference of the COD. This results in positive outliers of α, as illustrated in Fig. 20. A mean of the AOD values of the day before *and* the day after would have smoothed the effect, or, for a set minimum number of values the day would be automatically removed from the data set. However, this specific day (September 3 2012) was eliminated during a manual quality control and not taken into account during the presented analysis.

Additionally, COD estimates were assigned to different cloud types. The cloud types were determined using all-sky images gathered from 2011 to 2013 with an hourly resolution. However, due to this low temporal resolution it was not possible to incorporate highly variable cloud situations into the analysis. Therefore, measurement periods were only considered, when at least two consecutive all-sky images showed the same cloud type. Derived COD values have been assigned to these single cloud events. The analysis was conducted for four cloud types only (Cirrus Ci, Cirrostratus Cs, Stratocumulus Sc, Altocumulus Ac), due to a limited number of COD retrievals per cloud type. Cirrus clouds (87 measurements) exhibit a narrow COD range from 0.17 to 0.72 with a median of 0.38 due to their optically and geometrically thin nature. The geometrically and optically thicker clouds Cs, Sc and Ac, however, exhibit broader COD distributions. The COD of Cs clouds (264 measurements) ranges from 0.21 to 2.37 and has a median of 0.79, for Sc (84 measurements) the COD ranges from 0.40 to 2.37

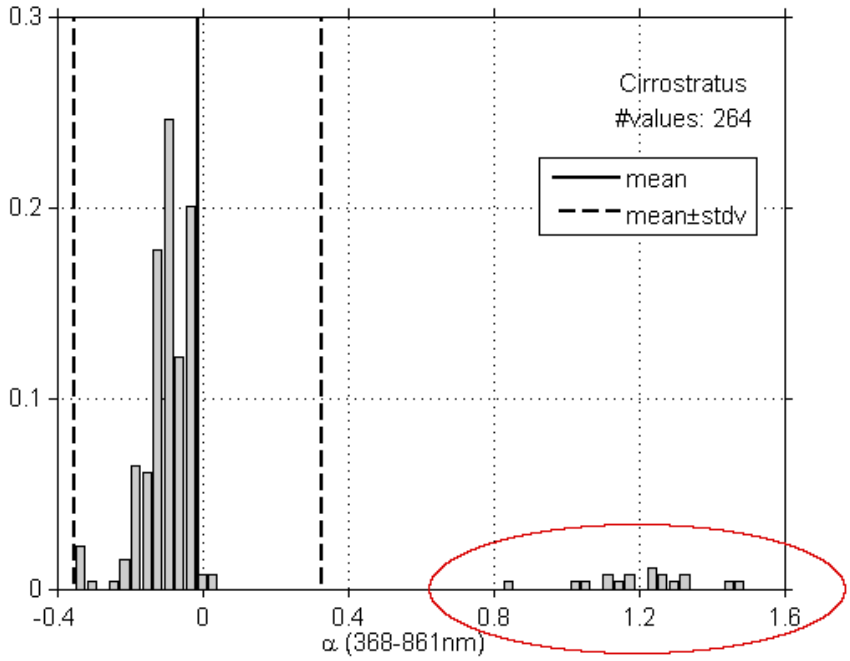

Figure 20: Histogram of the Ångström exponent α, calculated with the wavelengths 368, 412, 501 and 861 nm, for Cirrostratus clouds. An inaccurate derivation of the mean AOD for the COD values on September 3 2012 led to positive outliers in the Ångström exponent (red ellipse). These were manually removed for the analysis.

with a median of 1.03 and for Altocumulus (68 measurements) from 0.17 to 2.19 with a median of 0.89.

From the examination of optically thin Arctic clouds with infrared radiance and lidar cloud boundary observations Turner (2005) derived COD frequency distributions of liquid water, mixed-phase and ice clouds (Fig. 9 in his work). The COD frequency distributions correlate well with the here presented COD distributions. Combining the histograms of Cirrus and Cirrostratus clouds in Fig. 15a and b yields nearly identical results compared to the ice cloud COD histograms of Turner (2005) in the COD range from zero to 2.5. Moreover, the equipartitioned COD histogram of Ac and Sc with a small increase towards smaller CODs is comparable to the results of Turner (2005) for liquid water and mixed-phase clouds. Therefore, it can be concluded that the classification into several cloud types conducted in the presented thesis shows reasonable results.

In order to increase the accuracy of the cloud type assignment, a higher temporal resolution of the all-sky images, which form the basis for the cloud type discrimination, would be desirable. On the other hand, an increased number of all-sky images would also result in increased efforts to manually categorize the cloud types. Furthermore, investigating a longer time series of all-sky images would yield more measurements and lead to more reliable results. Cloud base height information, inferred by an additional

instrument like a ceilometer, would further improve cloud type assignment. This is especially valid for differentiation between, for example, Sc and Ac clouds.

The empirical Ångström turbidity formula

$$\tau_a = \beta \cdot \lambda^{-\alpha}$$

is originally used to derive the Ångström exponent α from *aerosol optical depth* measurements. To the author's knowledge this approach has not been employed for COD retrievals so far. However, in the presented thesis the derived *CODs* in the wavelength channels 368, 412, 501 and 861 nm are used to determine the Ångström exponent α for clouds. The α values range from -0.82 to 1.99 for all analyzed measurements with clouds obscuring the sun. 80% of all α from cloud-contaminated measurements lie between -0.23 and 0.1. With respect to different cloud types, the values of α range from -0.2 to -0.04 with a median of -0.11 for Ci, Cirrostratus clouds exhibit some slightly positive values, α ranges from -0.22 to 0.02 with a median of -0.09. Stratocumulus clouds show nearly equipartitioned α values over the range from -0.36 to 0.05 with a median of -0.17 and Ac clouds have a similar range with a minimum of -0.33, a maximum of -0.05 and a median of -0.15. However the Ac α histogram has a slight peak at about -0.1. A possible reason for this is that Ac clouds can appear as mixed-phase clouds. Additionally, the curvature parameter γ was calculated. The value range of γ for all cloud-contaminated measurements is from -3.02 to 6.52 with a mean of 0.02. However, the 10^{th}-percentile is at -0.06 and the 90^{th}-percentile at 0.09, i.e. for the majority of the retrievals gamma was nearly zero. Therefore, it has not been taken into account any further during the presented analysis.

In aerosol research only few authors mention negative α values and even fewer provide an explanation for this phenomenon. Moreover, no studies are known to the author that examine α for cloud measurements. Arola and Koskela (2004) and Estupinan (2006) state that occurring negative Ångström exponents (for aerosol measurements) are connected with experimental and statistical uncertainties. Miller et al. (2003) investigated aerosol optical properties in the VIS and NIR spectral ranges and found that negative α values were caused by differential absorption. They assume, that for this effect a large number of hydrometeors must be present in an otherwise clear atmosphere (low AOD). Additionally, they state that ice and liquid water particles have to be sufficiently large to have a minor impact on scattering in the VIS, but a major impact on absorption in the NIR part of the spectrum. However, the effect of absorption was not considered in the presented thesis because, according to Petty (2006), it is negligibly small compared to scattering in the VIS and NIR range for particles in the size of cloud hydrometeors. Miller et al. (2003) and Toledano et al. (2007) hint that precipitation in the measuring area or cloud contamination of the AOD measurements could result in negative α values but they do not go into further detail. Jarosławski et al. (2003)

examined AOD measurements in the UV spectral range and state that negative α are not caused by statistical or instrumental errors (in contrast to, e.g., Arola and Koskela 2004; Estupinan 2006). Jarosławski et al. (2003) mention that a negative α might be caused by Mie scattering for a specific combination of wavelengths, particle radii and refractive indices. This hypothesis has been examined in more detail and confirmed within the presented thesis.

In the context of this thesis the negative Ångström parameter α is attributed to a spectral difference of extinction efficiency for cloud hydrometeors in the VIS and NIR spectral range. The extinction efficiency of cloud drops in the typical size range of Sc and Ac clouds (2 to 12 μm) is increasing with increasing wavelength. This is especially evident for the 861 nm wavelength channel in comparison to the other wavelengths of 368, 412 and 501 nm. These spectral differences of the extinction efficiency cause negative α values.

In the base of Ci clouds small spatial ice crystals like bullet rosettes and aggregates with sizes of approximately 15 μm can be found. These show a similar extinction efficiency behavior like liquid cloud drops. However, spectral differences in extinction efficiency are smaller and absolute values of the extinction efficiency are lower for these types of hydrometeors. Cirrostratus and the top part of Cirrus clouds comprise mainly of droxtals and columns, and in Ci cloud bases larger aggregates can be found. Larger ice crystals ($\approx 200\ \mu m$) and small droxtals, columns and plates show nearly no spectral dependency of the extinction efficiency which yields $\alpha = 0$. Combining these two effects connected to ice crystals aims a zero to slightly negative Ångström exponent for ice clouds.

The different behavior of ice and water clouds leads to two distinctive modes in the COD-α-relation (Fig. 14). The upper mode ($\alpha \approx -0.1$) is connected to ice clouds, while the lower mode ($\alpha \approx -0.3$) is connected to the presence of water clouds. If the COD-α-relation for *different cloud types* is examined (Fig. 17) a negative trend of α with increasing COD is apparent for water clouds. This behavior is hypothesized to be caused by multiple scattering (enhanced with increasing COD) that might further increase the spectral differences of the extinction efficiency, leading to a decreasing α. However, the effect of multiple scattering in clouds has not been concretely identified in the presented study. Min et al. (2004), for example, implemented a correction for forward scattering in their approach to derive the COD. In a future approach this might be a useful extension to the herein presented COD retrieval.

The approach of this study determining the COD by the described approach is advantageous in several ways: The COD is inferred from measurements by ground-based sun photometers. Sun photometers are already deployed at numerous sites globally, for example, as part of the AERONET or GAW measurement networks. Therefore, existing measurement sites and instruments can be used to incorporate the proposed

approach to access additional COD retrievals. Moreover, it is possible to infer AOD *and* COD, although alternating, nearly simultaneously, which is a rare setup. To the author's knowledge, this is also possible with the approach described by Chiu et al. (2007), using a micropulse lidar to infer AOD and COD nearly simultaneously. Marshak et al. (2004) and Chiu et al. (2010) proposed an approach to use zenith radiance measurements gathered by AERONET instrumentation to infer COD. To use their approach, instrumentation needs to be capable to switch between zenith measurements and sun-tracking direct solar measurements. The AERONET sun photometers can switch into *cloud mode* when clouds obscure the sun, to measure zenith radiance. However, the cloud mode at several sites only covers CODs $\gtrsim 3$ (Chiu et al. 2010). Therefore, the herein presented COD retrieval covering optically thin clouds with COD< 3 would be a useful complement to the cloud mode measurements proposed by Chiu et al. (2010). Min et al. (2004) developed a retrieval method which uses direct solar beam measurements to retrieve the COD of thin clouds. Regarding the instrumentation and type of measurements, their approach is comparable to the one presented herein.

Direct solar irradiance measurements have, like zenith radiance measurements, the advantage that the temporal variability of cloud properties is better captured than it is by hemispheric measurements. The latter technique retrieves quantities averaged over the sky hemisphere, whereas the approach used herein can infer the temporal course of the optical parameters within a limited FOV, hence, more locally.

In summary, it is possible to derive cloud optical parameters from sun photometers' direct solar irradiance measurements using the approach COD = OD − mean(AOD). However, due to the sensitivity of the sun photometer sensor only optically thin clouds can be investigated. The cloud type determination with all-sky images delivered reasonable results. A discrimination between the thin cloud types on the basis of COD, the Ångström exponent α and the curvature parameter γ is not possible. The latter, γ, is equals zero for nearly all cloud contaminated measurements and, therefore, not considered. Parameter α describes the spectral differences of the CODs and is primarily negative. In dependency of the COD, α is nearly constant for ice clouds Ci and Cs, but decreasing with increasing COD for water clouds Sc and Ac. It is hypothesized that this is caused by nearly not changing (ice clouds) and increasing (water clouds) spectral extinction efficiency differences due to multiple scattering in optically thicker clouds.

Bibliography

Angström, A., 1929: On the atmospheric transmission of Sun radiation and on dust in the air. *Geogr. Ann.*, **11**, 256–166.

Angström, A., 1964: The parameters of atmospheric turbidity. *Tellus*, **16 (1)**, 64–75.

Arola, A., and T. Koskela, 2004: On the sources of bias in aerosol optical depth retrieval in the UV range. *J. Geophys. Res.*, **109 (D8)**, doi:10.1029/2003JD004375.

Barker, H. W., T. J. Curtis, E. Leontieva, and K. Stamnes, 1998: Optical Depth of Overcast Cloud across Canada: Estimates Based on Surface Pyranometer and Satellite Measurements. *J. Climate*, **11**, 2980–2994, doi:10.1175/1520-0442(1998)011⟨2980:ODOOCA⟩2.0.CO;2.

Barker, H. W., and D. Liu, 1995: Inferring Optical Depth of Broken Clouds from Landsat Data. *J. Climate*, **8**, 2620–2630, doi:10.1175/1520-0442(1995)008⟨2620:IODOBC⟩2.0.CO;2.

Barker, H. W., and A. Marshak, 2001: Inferring Optical Depth of Broken Clouds above Green Vegetation Using Surface Solar Radiometric Measurements. *J. Atmos. Sci.*, **58**, 2989–3006, doi:10.1175/1520-0469(2001)058⟨2989:IODOBC⟩2.0.CO;2.

Barnard, J. C., and C. N. Long, 2004: A Simple Empirical Equation to Calculate Cloud Optical Thickness Using Shortwave Broadband Measurements. *J. Appl. Meteor.*, **43**, 1057–1066, doi:10.1175/1520-0450(2004)043⟨1057:ASEETC⟩2.0.CO;2.

Beauchamp, J., A. Wisthaler, W. Grabmer, C. Neuner, A. Weber, and A. Hansel, 2004: Short-term measurements of co, no, no2, organic compounds and {PM10} at a motorway location in an austrian valley. *Atmos. Environ.*, **38 (16)**, 2511 – 2522, doi:10.1016/j.atmosenv.2004.01.032.

Beaulne, A., H. W. Barker, and J.-P. Blanchet, 2005: Estimating Cloud Optical Depth from Surface Radiometric Observations: Sensitivity to Instrument Noise and Aerosol Contamination. *J. Atmos. Sci.*, **62**, 4095–4104, doi:10.1175/JAS3544.1.

Bender, F., H. Rodhe, R. Charlson, A. Ekman, and N. Loeb, 2006: 22 views of the global albedo-comparison between 20 gcms and two satellites. *Tellus*, **58A**, 320–330, doi:10.1111/j.1600-0870.2006.00181.x.

Blumthaler, M., W. Ambach, and A. Blasbichler, 1996: Measurements of the Spectral Aerosol Optical Depth using a Sun Photometer. *Theor. Appl. Climatol.*, **57**, 95–101.

Bodhaine, B. A., N. B. Wood, E. G. Dutton, and J. R. Slusser, 1999: On rayleigh optical depth calculations. *J. Atmos. Oceanic Technol.*, **16 (11)**, 1854–1861, doi: 10.1175/1520-0426(1999)016⟨1854:ORODC⟩2.0.CO;2.

Boers, R., 1997: Simultaneous retrievals of cloud optical depth and droplet concentration from solar irradiance and microwave liquid water path. *J. Geophys. Res.*, **102**, 29 881–29 891, doi:10.1029/97JD02494.

Boers, R., A. van Lammeren, and A. Feijt, 2000: Accuracy of Cloud Optical Depth Retrievals from Ground-Based Pyranometers. *J. Atmos. Oceanic Technol.*, **17**, 916–927, doi:10.1175/1520-0426(2000)017⟨0916:AOCODR⟩2.0.CO;2.

Boucher, O., 2015: *Atmospheric Aerosols. Properties and Climate Impacts.* Springer Netherlands, 311 pp., doi:10.1007/978-94-017-9649-1.

Chiu, J. C., C.-H. Huang, A. Marshak, I. Slutsker, D. M. Giles, B. N. Holben, Y. Knyazikhin, and W. J. Wiscombe, 2010: Cloud optical depth retrievals from the Aerosol Robotic Network (AERONET) cloud mode observations. *J. Geophys. Res.*, **115**, doi:10.1029/2009JD013121.

Chiu, J. C., A. Marshak, W. J. Wiscombe, S. C. Valencia, and E. J. Welton, 2007: Cloud Optical Depth Retrievals From Solar Background "Signals"; of Micropulse Lidars. *Geosc. Remote Sens. Lett.*, **4**, 456–460, doi:10.1109/LGRS.2007.896722.

Comstock, J. M., and K. Sassen, 2001: Retrieval of Cirrus Cloud Radiative and Backscattering Properties Using Combined Lidar and Infrared Radiometer (LIRAD) Measurements. *J. Atmos. Oceanic Technol.*, **18**, 1658–1673, doi:10.1175/1520-0426(2001)018⟨1658:ROCCRA⟩2.0.CO;2.

Comstock, J. M., and Coauthors, 2007: An intercomparison of microphysical retrieval algorithms for upper-tropospheric ice clouds. *Bull. Amer. Meteor. Soc.*, **88 (2)**, 191–204, doi:10.1175/BAMS-88-2-191.

Davis, A. B., and A. Marshak, 2010: Solar radiation transport in the cloudy atmosphere: a 3D perspective on observations and climate impacts. *Rep. Prog. Phys.*, **73**, 026 801, URL http://stacks.iop.org/0034-4885/73/i=2/a=026801.

Eck, T. F., B. N. Holben, J. S. Reid, O. Dubovik, A. Smirnov, N. T. O'Neill, I. Slutsker, and S. Kinne, 1999: Wavelength dependence of the optical depth of biomass burning, urban, and desert dust aerosols. *J. Geophys. Res.*, **104 (D24)**, 31 333–31 349, doi: 10.1029/1999JD900923.

Estupinan, J., 2006: The direct influence of aerosols on uv irradiance and the development of a synthetic current uv index. PhD dissertation, Georgia Institute of Technology, 168 pp.

Finger, F., and Coauthors, 2016: Spectral optical layer properties of cirrus from collocated airborne measurements and simulations. *Atmos. Chem. Phys.*, **16 (12)**, 7681–7693, doi:10.5194/acp-16-7681-2016.

Forster, P., and Coauthors, 2007: Changes in atmospheric constituents and in radiative forcing. *Climate Change 2007: The Physical Science Basis. Contribution of Working Group I to the Fourth Assessment Report of the Intergovernmental Panel on Climate Change*, S. Solomon, D. Qin, M. Manning, Z. Chen, M. Marquis, K. B. Averyt, M. Tignor, and H. L. Miller, Eds., Cambridge University Press, 129–234.

Fu, Q., 1996: An Accurate Parameterization of the Solar Radiative Properties of Cirrus Clouds for Climate Models. *J. Climate*, **9**, 2058–2082, doi:10.1175/1520-0442(1996)009⟨2058:AAPOTS⟩2.0.CO;2.

Gobbi, G. P., Y. J. Kaufman, I. Koren, and T. F. Eck, 2007: Classification of aerosol properties derived from AERONET direct sun data. *Atmos. Chem. Phys.*, **7 (2)**, 453–458, doi:10.5194/acp-7-453-2007.

Gohm, A., and Coauthors, 2009: Air Pollution Transport in an Alpine Valley: Results From Airborne and Ground-Based Observations. *Bound.–Layer Meteor.*, **131**, 441–463.

Grabner, S., 2003: Messung der Aerosol-Extinktion mit einem Präzisions Filter Radiometer PFR in Innsbruck und Analyse der Daten. Dipoma's thesis, Institute for Meteorology and Geophysics, University of Innsbruck, 86 pp.

Grenfell, T. C., and S. G. Warren, 1999: Representation of a nonspherical ice particle by a collection of independent spheres for scattering and absorption of radiation. *J. Geophys. Res.: Atmos.*, **104 (D24)**, 31 697–31 709.

Guerrero-Rascado, J. L., M. J. Costa, A. M. Silva, and F. Olmo, 2011: An approach to the retrieval of thin cloud optical depth from a cimel sun-photometer. *Proceedings of the Global Conference on Global Warming*, Lisbon, Portugal, 1–7, [Available online at http://hdl.handle.net/10174/3246.].

Harnisch, F., A. Gohm, A. Fix, R. Schnitzhofer, A. Hansel, and B. Neininger, 2009: Spatial distribution of aerosols in the Inn Valley atmosphere during wintertime. *Meteor. Atmos. Phys.*, **103**, 223–235.

Holben, B. N., and Coauthors, 1998: AERONET: A federated instrument network and data archive for aerosol characterization. *Remote Sens. Environ.*, **66**, 1–16.

Holben, B. N., and Coauthors, 2001: An emerging ground-based aerosol climatology: Aerosol optical depth from AERONET. *J. Geophys. Res.*, **106 (D11)**, 12 067–12 097, doi:10.1029/2001JD900014.

Hu, Y. X., and K. Stamnes, 1993: An Accurate Parameterization of the Radiative Properties of Water Clouds Suitable for Use in Climate Models. *J. Climate*, **6**, 728–742, doi:10.1175/1520-0442(1993)006⟨0728:AAPOTR⟩2.0.CO;2.

Illingworth, A. J., and Coauthors, 2007: Cloudnet. *Bull. Amer. Meteor. Soc.*, **88**, 883–898, doi:10.1175/BAMS-88-6-883.

Ingold, T., C. Mätzler, N. Kämpfer, and A. Heimo, 2001: Aerosol optical depth measurements by means of a sun photometer network in switzerland. *J. Geophys. Res.: Atmos.*, **106 (D21)**, 27 537–27 554, doi:10.1029/2000JD000088.

IPCC, 2007: *Climate Change 2007: The Physical Science Basis*. Cambridge University Press, 996 pp.

Iqbal, M., 1983: *An Introduction to Solar Radiation*. Academic Press Canada, 390 pp.

Jarosławski, J., J. W. Krzyścin, S. Puchalski, and P. Sobolewski, 2003: On the optical thickness in the UV range: Analysis of the ground-based data taken at Belsk, Poland. *J. Geophys. Res.: Atmos.*, **108 (D23)**, doi:10.1029/2003JD003571, 4722.

Kasten, F., 1965: A new table and approximation formula for the relative optical air mass. *Theor. Appl. Climatol.*, **14**, 206–223.

Kasten, F., and A. T. Young, 1989: Revised optical air mass tables and approximation formula. *Appl. Opt.*, **28**, 4735–4738.

Kaufman, Y. J., 1993: Aerosol optical thickness and atmospheric path radiance. *J. Geophys. Res.: Atmos.*, **98**, 2677–2692.

Kinne, S., and Coauthors, 1997: Cirrus cloud radiative and microphysical properties from ground observations and in situ measurements during FIRE 1991 and their application to exhibit problems in cirrus solar radiative transfer modeling. *J. Atmos. Sci.*, **54 (18)**, 2320–2344.

Kokhanovsky, A., 2004: Optical properties of terrestrial clouds. *Earth-Sc. Rev.*, **64 (3)**, 189–241.

Komhyr, W. D., R. D. Grass, and R. K. Leonard, 1989: Dobson spectrophotometer 83 - A standard for total ozone measurements, 1962–1987. *J. Geophys. Res.*, **94**, 9847–9861.

Kraus, H., 2004: *Die Atmosphäre der Erde*. 3rd ed., Springer-Verlag Berlin Heidelberg, 427 pp.

Kreuter, A., S. Wuttke, and M. Blumthaler, 2013: Improving Langley calibrations by reducing diurnal variations of aerosol Ångström parameters. *Atmos. Meas. Tech. Discuss.*, **6**, 99–103.

Leontieva, E., and K. Stamnes, 1994: Estimations of cloud optical thickness from ground-based measurements of incoming solar radiation in the Arctic. *J. Climate*, **7**, 566–578.

Leontieva, E., and K. Stamnes, 1996: Remote sensing of cloud optical properties from ground-based measurements of transmittance: A feasibility case. *J. Appl. Meteor.*, **35**, 2012–2022.

Liou, K., 2002: *An Introduction to Atmospheric Radiation*. International Geophysics series, Academic Press.

Loeb, N. G., and J. A. Coakley, 1998: Inference of Marine Stratus Cloud Optical Depths from Satellite Measurements: Does 1D Theory Apply? *J. Climate*, **11**, 215–233, doi:10.1175/1520-0442(1998)011⟨0215:IOMSCO⟩2.0.CO;2.

Lohmann, U., F. Lüönd, and F. Mahrt, 2016: *An Introduction to Clouds: From the Microscale to Climate*. Cambridge University Press.

Marshak, A., Y. Knyazikhin, A. B. Davis, W. J. Wiscombe, and P. Pilewskie, 2000: Cloud-vegetation interaction: Use of normalized difference cloud index for estimation of cloud optical thickness. *Geophys. Res. Lett.*, **27**, 1695–1698, doi: 10.1029/1999GL010993.

Marshak, A., Y. Knyazikhin, K. D. Evans, and W. J. Wiscombe, 2004: The "RED versus NIR" Plane to Retrieve Broken-Cloud Optical Depth from Ground-Based Measurements. *J. Atmos. Sci.*, **61**, 1911–1925, doi:10.1175/1520-0469(2004)061⟨1911:TRVNPT⟩2.0.CO;2.

Matrosov, S. Y., M. D. Shupe, A. J. Heymsfield, and P. Zuidema, 2003: Ice cloud optical thickness and extinction estimates from radar measurements. *J. Appl. Meteor.*, **42**, 1584–1597, doi:10.1175/1520-0450(2003)042%3C1584:ICOTAE%3E2.0.CO;2.

Michalsky, J. J., J. A. Schlemmer, W. E. Berkheiser, J. L. Berndt, L. C. Harrison, N. S. Laulainen, N. R. Larson, and J. C. Barnard, 2001: Multiyear measurements of aerosol optical depth in the Atmospheric Radiation Measurement and Quantitative Links programs. *J. Geophys. Res.*, **106**, 12 099–12 107, doi:10.1029/2001JD900096.

Michalsky, J. J., and Coauthors, 2006: Shortwave radiative closure studies for clear skies during the Atmospheric Radiation Measurement 2003 Aerosol Intensive Observation Period. *J. Geophys. Res.*, **11**, doi:10.1029/2005JD006341.

Miller, M. A., R. M. Reynolds, and M. J. Bartholomew, 2003: NASA/TM-2003-211622. SIMBIOS Project 2002 Annual Report. Fargion, Giulietta S. and McClain, Charles R., http://oceancolor.gsfc.nasa.gov/cmsdocs/technical_documents/simbios/simbios_annual_2002.pdf.

Min, Q., and L. C. Harrison, 1996: Cloud properties derived from surface MFRSR measurements and comparison with GOES results at the ARM SGP Site. *Geophys. Res. Lett.*, **23**, 1641–1644, doi:10.1029/96GL01488.

Min, Q., E. Joseph, and M. Duan, 2004: Retrievals of thin cloud optical depth from a multifilter rotating shadowband radiometer. *J. Geophys. Res.*, **109**, n/a–n/a, doi:10.1029/2003JD003964.

NASA, cited 2016a: Aerosol Robotic Network (AERONET), available online at http://aeronet.gsfc.nasa.gov/.

NASA, cited 2016b: Ozone Monitoring Instrument (OMI), available online at http://www.nasa.gov/mission_pages/aura/spacecraft/omi.html.

O'Neill, N. T., A. Ignatov, B. N. Holben, and T. F. Eck, 2000: The lognormal distribution as a reference for reporting aerosol optical depth statistics; Empirical tests using multi-year, multi-site AERONET Sunphotometer data. *Geophys. Res. Lett.*, **27 (20)**, 3333–3336, doi:10.1029/2000GL011581, URL http://dx.doi.org/10.1029/2000GL011581.

Parungo, F., 1995: Ice crystals in high clouds and contrails. *Atmos. Res.*, **38 (1)**, 249–262, doi:http://dx.doi.org/10.1016/0169-8095(94)00096-V.

Peterlin, D., 2006: Sonnenscheindauer und Globalstrahlung in Innsbruck. Master's thesis, University of Innsbruck, 96 pp.

Peterson, J. T., E. C. Flowers, G. J. Berri, C. L. Reynolds, and J. H. Rudisill, 1981: Atmospheric turbidity over central north carolina. *J. Appl. Meteor.*, **20 (3)**, 229–241, doi:10.1175/1520-0450(1981)020⟨0229:ATOCNC⟩2.0.CO;2.

Petty, G. W., 2006: *A first course in Atmospheric Radiation.* Sundog Publishing, Madison, Wisconsin.

Pogodi, R., cited 2016: Wetterarchiv in Innsbruck (Flughafen), available online at http://rp5.ru/Wetterarchiv_in_Innsbruck_(Flughafen).

Randall P. Julander, cited 2016: Optical Properties of Snow, available online at http://www.civil.utah.edu/~cv5450/Remote/AVIRIS/optics.html.

Raschke, E., 1993: Radiation-cloud-climate interaction. *Energy and Water Cycles in the Climate System*, E. Raschke, and D. Jacob, Eds., Springer-Verlag, 70–92.

Rawlins, F., and J. S. Foot, 1990: Remotely Sensed Measurements of Stratocumulus Properties during FIRE Using the C130 Aircraft Multi-channel Radiometer. *J. Atmos. Sci.*, **47**, 2488–2504, doi:10.1175/1520-0469(1990)047⟨2488:RSMOSP⟩2.0.CO;2.

Rossow, W. B., and R. A. Schiffer, 1991: ISCCP Cloud Data Products. *Bull. Amer. Meteor. Soc.*, **72**, 2–20, doi:10.1175/1520-0477(1991)072⟨0002:ICDP⟩2.0.CO;2.

Schuster, G. L., O. Dubovik, and B. N. Holben, 2006: Angstrom exponent and bimodal aerosol size distributions. *J. Geophys. Res.: Atmos.*, **111 (D7)**.

Segal-Rosenheimer, M., P. B. Russell, J. M. Livingston, S. Ramachandran, J. Redemann, and B. A. Baum, 2013: Retrieval of cirrus properties by sun photometry: A new perspective on an old issue. *J. Geophys. Res.*, **118**, 4503–4520, doi:10.1002/jgrd.50185.

Seibert, P., H. Feldmann, B. Neininger, M. Bäumle, and T. Trickl, 2000: South foehn and ozone in the Eastern Alps - case study and climatological aspects. *Atmos. Environ.*, **34**, 1379–1394.

Shupe, M. D., J. M. Comstock, D. D. Turner, and G. G. Mace, 2016: Cloud Property Retrievals in the ARM Program. *Meteor. Monogr.*, **57**, 19.1–19.20, doi:10.1175/AMSMONOGRAPHS-D-15-0030.1.

Smirnov, A., B. Holben, T. Eck, O. Dubovik, and I. Slutsker, 2000: Cloud-screening and quality control algorithms for the {AERONET} database. *Remote Sens. Environ.*, **73 (3)**, 337 – 349, doi:http://dx.doi.org/10.1016/S0034-4257(00)00109-7.

Sourdeval, O., L. C.-Labonnote, A. J. Baran, and G. Brogniez, 2015: A methodology for simultaneous retrieval of ice and liquid water cloud properties. Part I: Information content and case study. *Quart. J. Roy. Meteor. Soc.*, **141**, 870–882, doi:10.1002/qj.2405.

Stephens, G. L., 1994: *Remote Sensing of the Lower Atmosphere: An Introduction.* Oxford University Press, New York, 521 pp.

Stephens, G. L., 2005: Cloud Feedbacks in the Climate System: A critical review. *J. Climate*, **18**, 237–273, doi:10.1175/JCLI-3243.1.

Stephens, G. L., S.-C. Tsay, P. W. Stackhouse Jr., and P. J. Flatau, 1990: The relevance of the microphysical and radiative properties of cirrus clouds to climate and climate feedback. *J. Atmos. Sci.*, **47**, 1742–1753.

Stokes, G. M., and S. E. Schwartz, 1994: The Atmospheric Radiation Measurement (ARM) Program: Programmatic Background and Design of the Cloud and Radiation Test Bed. *Bull. Amer. Meteor. Soc.*, **75**, 1201–1221, doi:10.1175/1520-0477(1994)075⟨1201:TARMPP⟩2.0.CO;2.

Tian, B., and V. Ramanathan, 2002: Role of tropical clouds in surface and atmospheric energy budget. *J. Climate*, **15**, 296–305.

Toledano, C., V. E. Cachorro, A. Berjon, A. M. de Frutos, M. Sorribas, B. A. de la Morena, and P. Goloub, 2007: Aerosol optical depth and Ångström exponent climatology at el arenosillo aeronet site (huelva, spain). *Quart. J. Roy. Meteor. Soc.*, **133 (624)**, 795–807, doi:10.1002/qj.54.

Turner, D. D., 2005: Arctic Mixed-Phase Cloud Properties from AERI Lidar Observations: Algorithm and Results from SHEBA. *J. Appl. Meteor.*, **44**, 427–444, doi:10.1175/JAM2208.1.

Turner, D. D., and Coauthors, 2004: The QME AERI LBLRTM: A closure experiment for downwelling high spectral resolution infrared radiance. *J. Atmos. Sci.*, **61**, 2657–2675.

Turner, D. D., and Coauthors, 2007: Thin Liquid Water Clouds: Their Importance and Our Challenge. *Bull. Amer. Meteor. Soc.*, **88**, 177–190, doi:10.1175/BAMS-88-2-177.

Valks, P., G. Pinardi, A. Richter, J.-C. Lambert, N. Hao, D. Loyola, M. Van Roozendael, and S. Emmadi, 2011: Operational total and tropospheric NO2 column retrieval for GOME-2. *Atmos. Meas. Tech. Discuss.*, **4 (2)**, 1617–1676.

Vogelmann, A. M., and Coauthors, 2012: Racoro Extended-Term Aircraft Observations of Boundary Layer Clouds. *Bull. Amer. Meteor. Soc.*, **93**, 861–878, doi:10.1175/BAMS-D-11-00189.1.

Wallace, J., and P. Hobbs, 2006: *Atmospheric Science: An Introductory Survey.* International Geophysics, Elsevier Science, URL https://books.google.at/books?id=HZ2wNtDOU0oC.

Wang, T., and Q. Min, 2008: Retrieving optical depths of optically thin and mixed-phase clouds from MFRSR measurements. *J. Geophys. Res.*, **113**, doi:10.1029/2008JD009958.

Wehrli, C., 2008: *Precision Filter Radiometer Documentation*. ftp://ftp.pmodwrc.ch/pub/worcc/PFRManual.pdf, World Radiation Center Davos.

Wendisch, M., and P. Yang, 2012: *Theory of Atmospheric Radiative Transfer*. WILEY-VCH Verlag, 366 pp.

Wielicki, B. A., E. F. Harrison, R. D. Cess, M. D. King, and D. A. Randall, 1995: Mission to Planet Earth: Role of Clouds and Radiation in Climate. *Bull. Amer. Meteor. Soc.*, **76**, 2125–2153, doi:10.1175/1520-0477(1995)076⟨2125:MTPERO⟩2.0.CO;2.

WMO, cited 2016: GAW Aerosol Research, available online at http://www.wmo.int/pages/prog/arep/gaw/aerosol.htm.

Wuttke, S., A. Kreuter, and M. Blumthaler, 2012: Aerosol Climatology in an Alpine Valley. *J. Geophys. Res.*, **117**.

Yang, P., L. Bi, B. A. Baum, K.-N. Liou, G. W. Kattawar, M. I. Mishchenko, and B. Cole, 2013: Spectrally consistent scattering, absorption, and polarization properties of atmospheric ice crystals at wavelengths from 0.2 to 100 μm. *J. Atmos. Sci.*, **70 (1)**, 330–347, doi:10.1175/JAS-D-12-039.1, URL http://dx.doi.org/10.1175/JAS-D-12-039.1.

Zardi, D., and C. D. Whiteman, 2013: Diurnal mountain wind systems. *Mountain Weather Research and Forecasting: Recent Progress and Current Challenges*, K. F. Chow, F. S. De Wekker, and J. B. Snyder, Eds., Springer Netherlands, Dordrecht, 35–119, doi:10.1007/978-94-007-4098-3_2.

Zhang, M. H., and Coauthors, 2005: Comparing clouds and their seasonal variations in 10 atmospheric general circulation models with satellite measurements. *J. Geophys. Res.*, **110**, doi:10.1029/2004JD005021.

Acknowledgments

Dear Mario, dear Mr. Kuhn, I want to thank you for working with me on this interesting topic and supporting the becoming of this thesis. It was an honor for me to have the guidance of two such experienced scientists. Thank you for sharing your thoughts, thank you for your support, the motivation and your patience. Mr. Kuhn, you elated me especially for radiation topics early in my studies and I am glad about finishing university with a thesis in this field.

I also thank you, Martin Tiefengraber, for suggesting the collaboration with Mario and Mr. Kuhn in the first place and for the helpful discussions. Your enthusiasm in a tutorial you once gave was jointly responsible for my decision to study meteorology.

Lukas, Lena, Eva, Jock, Mia, Peter, Lukas, Anna, Luzian, Andi, Ella, Line, Thomas, I cannot say how happy I am to have friends like you supporting me in any situation. With you life is good.

Eidesstattliche Erklärung

Ich erkläre hiermit an Eides statt durch meine eigenhändige Unterschrift, dass ich die vorliegende Arbeit selbständig verfasst und keine anderen als die angegebenen Quellen und Hilfsmittel verwendet habe. Alle Stellen, die wörtlich oder inhaltlich den angegebenen Quellen entnommen wurden, sind als solche kenntlich gemacht.

Die vorliegende Arbeit wurde bisher in gleicher oder ähnlicher Form noch nicht als Magister-/Master-/Diplomarbeit/Dissertation eingereicht.

Datum	Unterschrift